Article:
Karimi, S., Barzegar, A., Al-Nadhari, A. et al. (4 more authors) (2025) Performance and failure mechanisms of interleaved E-glass/epoxy composites using knitted fiber-reinforced adhesive films. Polymer Composites. ISSN 0272-8397

https://doi.org/10.1002/pc.30127

Polymer Composites

WILEY | spe INSPIRING PLASTICS PROFESSIONALS

RESEARCH ARTICLE OPEN ACCESS

Performance and Failure Mechanisms of Interleaved E-Glass/Epoxy Composites Using Knitted Fiber-Reinforced Adhesive Films

Sasan Karimi[1,2] | Ali Barzegar[1,2] | Abdulrahman Al-Nadhari[1,2] | Andreas Kappel[3] | Christian Mittelstedt[3] | Hatice S. Sas[1,2,4] | Mehmet Yildiz[1,2]

[1]Faculty of Engineering and Natural Sciences, Department of Manufacturing Engineering, Sabanci University, Tuzla, Istanbul, Turkey | [2]Integrated Manufacturing Technologies Research and Application Center, Sabanci University, Tuzla, Istanbul, Turkey | [3]Department of Lightweight Construction and Structural Mechanics (LSM), Technische Universität Darmstadt, Darmstadt, Germany | [4]School of Mechanical, Aerospace and Civil Engineering, The University of Sheffield, Sheffield, UK

Correspondence: Hatice S. Sas (h.s.sas@sheffield.ac.uk)

Received: 17 February 2025 | **Revised:** 16 April 2025 | **Accepted:** 19 May 2025

Funding: The authors received no specific funding for this work.

Keywords: adhesive layer | fracture toughness | interleaving | mode-I and mode-II

ABSTRACT

In this study, an adhesive film with embedded knitted fibers is utilized as the interleaved layer to evaluate the effect of carrier fibers on delamination resistance, crack migration, and R-curve behavior in glass fiber/epoxy composites. The interaction between the knitted fibers within the adhesive layer and their integration with the main laminate matrix is examined. Mode-I and mode-II R-curves are determined using double cantilever beam (DCB) and end-notch-flexure (ENF) samples, respectively, with fractography used to characterize damage mechanisms and crack paths. The low viscosity of the epoxy matrix during pressurized curing causes redistribution of the knitted fibers and variations in the adhesive layer thickness along and across fiber orientations. This results in localized shifts in fracture mechanisms, leading to variations in toughness values. The weak interface between knit fibers and the adhesive layer matrix induces crack paths that cause significant fluctuations in G_{IC} values in Mode-I. The adhesive layer enhances fracture toughness by promoting a tortuous crack path, resulting in a 175.47% increase in G_{IC} during propagation and a 171.56% increase in G_{IIC} values during the initiation phase, respectively. The adhesive layer's thickness and fiber distribution, influenced by resin flow during manufacturing, played a critical role in fracture behavior. These findings provide insights into the mechanisms driving interlaminar toughening and highlight the potential of knitted fiber-reinforced adhesive films for improving delamination resistance in composite structures.

1 | Introduction

Fiber-reinforced polymer composites are widely used across diverse industries, including aerospace, automotive, and construction, due to their high specific stiffness, specific strength, low density, and exceptional durability. The directional dependence of strength and stiffness in composites, stemming from the tensile strength of fibers, can be tailored to match the loading boundary conditions of structural elements. In laminated composite materials, individual layers can be oriented to align their principal material directions with the primary load directions. This design approach maximizes the potential for high specific strength and stiffness, ensuring optimal laminate performance. However, laminating composite materials with different ply orientations introduces interlaminar shear and normal stresses due to property mismatches between

Summary

- Investigated knit fiber-supported adhesive's effect on composites' fracture toughness.
- Achieved a 171.56% G_{IIC} increase, promoting a tortuous crack path.
- Fluctuating G_{IC} values were observed due to localized variations in fracture caused by a weak knitted fiber-adhesive interface.
- Correlated macro fracture tests with SEM and optical microscopy images.
- Demonstrated knitted fiber-supported adhesives' potential to enhance delamination resistance.

individual laminae. These stresses can lead to interlaminar delamination and reduced out-of-plane properties, which are widely recognized as the predominant life-limiting failure mechanisms in composites. Consequently, enhancing interlaminar fracture toughness has emerged as a critical focus of ongoing research efforts [1–9].

The improvement of fracture toughness in laminated composites involves several techniques. These include the use of z-pins [10], refining the manufacturing process to enhance the quality of interlaminar bonding [11–14], and the development of toughened thermoset and thermoplastic matrices [15]. Other methods include the placement of interlayer nanofiber and microfiber veils [16–24], the application of nanoparticles, nanotubes, and short fibers [25–30], hybrid toughening methods with particles and veil fibers [1, 31–37], and optimizing lay-up sequences to minimize out-of-plane stresses. Adhesion surface treatment [38, 39], implementing three-dimensional weaving [40, 41], and applying interleaving and selective toughening with thermoset and thermoplastic adhesives or modified films are also employed [1, 42–51]. The primary objective of these methods is to delay crack propagation through high-energy dissipation mechanisms, such as matrix plasticity and shear deformation, crack arresting, crack tip deviation, and enhancing the fiber-matrix interface strength [1, 52, 53].

Among the above mentioned approaches, one promising way to increase the interlaminar toughness is placement of an adhesive layer of high toughness in the interlaminar area of laminated composites [45, 54]. This concept, known as the interleaving or interleaf method, involves introducing an additional layer at the interface between plies. The primary matrix and the interleaf layer work together to provide high stiffness and enhanced interlaminar toughness, respectively. A critical requirement for successful interleaving is the ductility of the interleaf resin, as it enables energy dissipation through plastic deformation and shear yielding, thereby enhancing fracture toughness. The interleaf resin achieves this by delaying crack initiation through plastic deformation within resin-rich domains, thereby enhancing the overall toughness of the composite. Moreover, interleaved composites have demonstrated superior behavior in terms of delamination resistance, in-plane shear strength, and compression after impact [3, 55–58]. Yet, the success of interleaving depends on several critical parameters. These include (i) the compatibility between the primary matrix and the interleaved resin, as a lack of bonding quality may lead to potential defects in the component, (ii) the toughness of the interleaf layer, which should ideally exceed that of the resin in the base laminates, and (iii) the thickness of the interleaf layer, where increased thickness results in a resin-rich layer and, consequently, a weight penalty [45, 55, 59]. Additionally, the mechanical properties and thickness of the interleaving resin should be carefully evaluated, and the manufacturing process must be optimized based on the specific application and the applied boundary forces for the final component [60].

Several studies in the literature have demonstrated the use of thermoset- and thermoplastic-based adhesives as interleaf layers [61]. In a study, Yasaee et al. [9] studied the use of various types of interlayer strips, including thermoplastic films, chopped fibers, and thermoset prepreg, investigating their effectiveness in enhancing the Mode-I fracture toughness. They specifically applied a thermoplastic polyimide interleaf, reporting 79% improvement in the critical energy release rate through Mode-I fracture toughness, G_{Ic}. In another study by Yasaee et al. [49], the use of a thermoset-based adhesive film as an interleaf resulted in a 112% increase in Mode-II fracture toughness, G_{IIc}, compared to reference samples. However, the authors highlighted the challenge of controlling the final thickness of the interleave layer during the manufacturing process, particularly due to resin/prepreg diffusion, which is a key issue in thermoset interleaving. According to Masters [61], there is an enhancement in the strain energy release of interleaved samples observed in both Mode-I and Mode-II tests, with the improvement being more pronounced in Mode-II. Additionally, the study concluded that interleaving is effective in reducing damage induced by impacts. Idress et al. [60, 62] examined design tools for interleaving, highlighting the importance of various factors. They fabricated composite sheets with different types of resin-rich layers (RRL) with different thicknesses. Alongside considering the relative thickness of the interleaf compared to the plastic deformation zone, they emphasized the critical role of selecting appropriate resins for RRL. Their results indicate that the effective interleaving is promoted by the closely matched toughness properties of the primary matrix resin and the interleaved resin. They concluded that a large mismatch between RRL and fiber-matrix toughness values results in an adhesive failure and poor toughening effect. These finding are also supported by Sela et al. [45]. Hojo et al. [63] investigated Mode-I and Mode-II loading for unidirectional CF/epoxy laminates with ionomer interleaf with different thicknesses. They reported significant improvement in both Mode-I and Mode-II fracture toughness. The microscopy images confirmed that the crack never propagates through non-toughened region which is the main reason behind the high toughness. In Resis and Reneker [64], an adhesive layer is applied as interleaf interlaminar layer along the free edges, and delamination is arrested by interleaf layer until final failure. In addition, fatigue loading interleaf layer reduces the crack propagation rate. Selective interleaving in stress concentration locations, such as holes and joints, has been successfully proven in many cases. However, a major limitation of interleaving is the resulting weight penalty. The discrete layer of interleaved resin reduces stiffness and

strength in the in-plane direction, requiring additional plies to maintain design properties [1]. However, literature lacks a comprehensive study for fracture performance of knit fiber supported epoxy-based adhesive layer application as interleave layer.

Although thermoset interleaves offer significant potential for enhancing composite toughness through diffusion and bonding with the primary matrix, they have been studied less extensively than their thermoplastic counterparts due to challenges in controlling interleaf thickness during manufacturing. Maintaining a uniform interleaf layer is crucial, as high pressure enhances bonding by minimizing voids; however, the low viscosity of the resin during hot pressing induces flow, leading to a reduction in interleaf thickness. This issue remains a critical challenge in thermoset composite interleaving, particularly in hot press processing.

In this study, interleaved glass fiber/epoxy composites were fabricated using compression molding in a hot press in one shot cycle. To the best knowledge of the authors, limited research has explored the use of high pressure for interleaved specimen manufacturing, despite its significant impact on the functionality of the interleave layer in enhancing fracture toughness. Two layers of adhesive film, each containing a knitted fiber carrier, were used as the interleave layer. The adhesive film resin was toughened epoxy-based, consistent with the main matrix, ensuring compatibility. However, during manufacturing in the hot press, at temperatures exceeding the glass transition temperature (T_g), both matrices exhibited a drop in viscosity and began to flow, complicating the creation of a uniformly thick interlaminar interleave layer. In the context of this study, the knitted fibers served a dual function. Firstly, they controlled the adhesive film thickness during high-pressure processing. The carrier fibers restricted the flow of the adhesive film's epoxy under high pressure, preventing excessive reduction in thickness. Secondly, during fracture, the knitted fibers contributed to the toughening effect by inducing crack tip deviation, facilitating load transfer between plies, and bridging the separation layers under both Mode-I and Mode-II loading conditions. Double cantilever beam (DCB) and end-notched flexure beam tests were conducted to provide a comprehensive understanding of failure mechanisms. The Mode-I and Mode-II test results were correlated with macro-level and micro-level analyses using optical microscopy images and SEM in a complementary manner. This study represents the first in the literature to utilize an adhesive film with knitted carrier fibers as an interleaf layer and to conduct an in-depth investigation of fracture mechanisms under Mode-I and Mode-II loading conditions. Furthermore, a correlation between load-bearing performance and fracture mechanisms is established.

2 | Material and Methods

2.1 | Materials and Sample Manufacturing

In this study, unidirectional E-glass/epoxy prepregs supplied by Krempel GmbH, Germany, are used as the prepreg materials. Additionally, a toughened thermoset adhesive film with a knitted fiber carrier, 3M-AF163-2K, supplied by 3M, is employed. Table 1 summarizes the specifications of the prepreg and adhesive film. To introduce a pre-crack for fracture testing, a 20-μm-thick PTFE film coated with a release agent is inserted between the adhesive layers. Prepreg layers are cut into 300 mm × 300 mm sheets and manually laminated with stacking sequences of $[0°]_{18}$ and $[0°]_{12}$ for fracture and tensile test samples, respectively. These sequences are selected to achieve the required final thickness for each test, in accordance with ASTM standards [65–67]. For the fracture test sample, two layers of adhesive film are inserted at the midplane between the 9th and 10th layers, while for the tensile test sample, the adhesive film is placed between the 6th and 7th layers. To ensure identical processing conditions are implemented for both reference and test specimens, adhesive films are applied to only half of the sheet during a single hot press cycle (Figure 1a). This approach allows for a rigorous comparison between the reference samples (denoted as REF, without an adhesive film) and the test samples (denoted as ALE, with an embedded adhesive layer as interleaf), as both are subjected to the same processing conditions. Figure 1b,c illustrate the stacking sequences for REF and ALE sections, along with the adhesive layer placement for fracture and tensile tests, respectively. For fracture test samples, the pre-crack length is set to 63 mm for both Mode-I and Mode-II tests using PTFE film (Figure 1a).

TABLE 1 | Prepreg and adhesive layer specifications.

Prepreg—KREMPEL GmbH (UD prepreg)	
Resin type	Epoxy resin
Fiber type	E-glass
Mass per unit area of fiber (g/m^2)	310
Mass per unit area of prepreg (g/m^2)	496
Fiber density (g/m^2)	2.54
Effective prepreg thickness (mm)	0.2
Fiber volume content (%)	60
Adhesive layer—3 M (Scotch-Weld AF 163–2 K film)	
Mass per unit area (g/cm^2)	219.7
Effective thickness (mm)	0.19
Color	Yellow
Stress intensity factor, K_{IC} ($MPa\,m^{1/2}$)	2.34
Tensile yield strength, σ_y (MPa)	36.22
Poisson ratio, υ	0.34

After the preforms with interleaved adhesive films are prepared, curing is carried out using a hot press process. The application of high pressure during curing plays a critical role in enhancing the fracture performance of interleaved composites. This is achieved through several mechanisms, including improved consolidation, stronger bonding, increased resin penetration into the knitted fibers of the interleave layer, and stabilization of fiber positioning. A hydraulic hot press with a one-sided oil-heated plate is used to manufacture the composite sheets, as shown in Figure 1d. A premanufactured mold is employed to apply uniformly distributed pressure across the

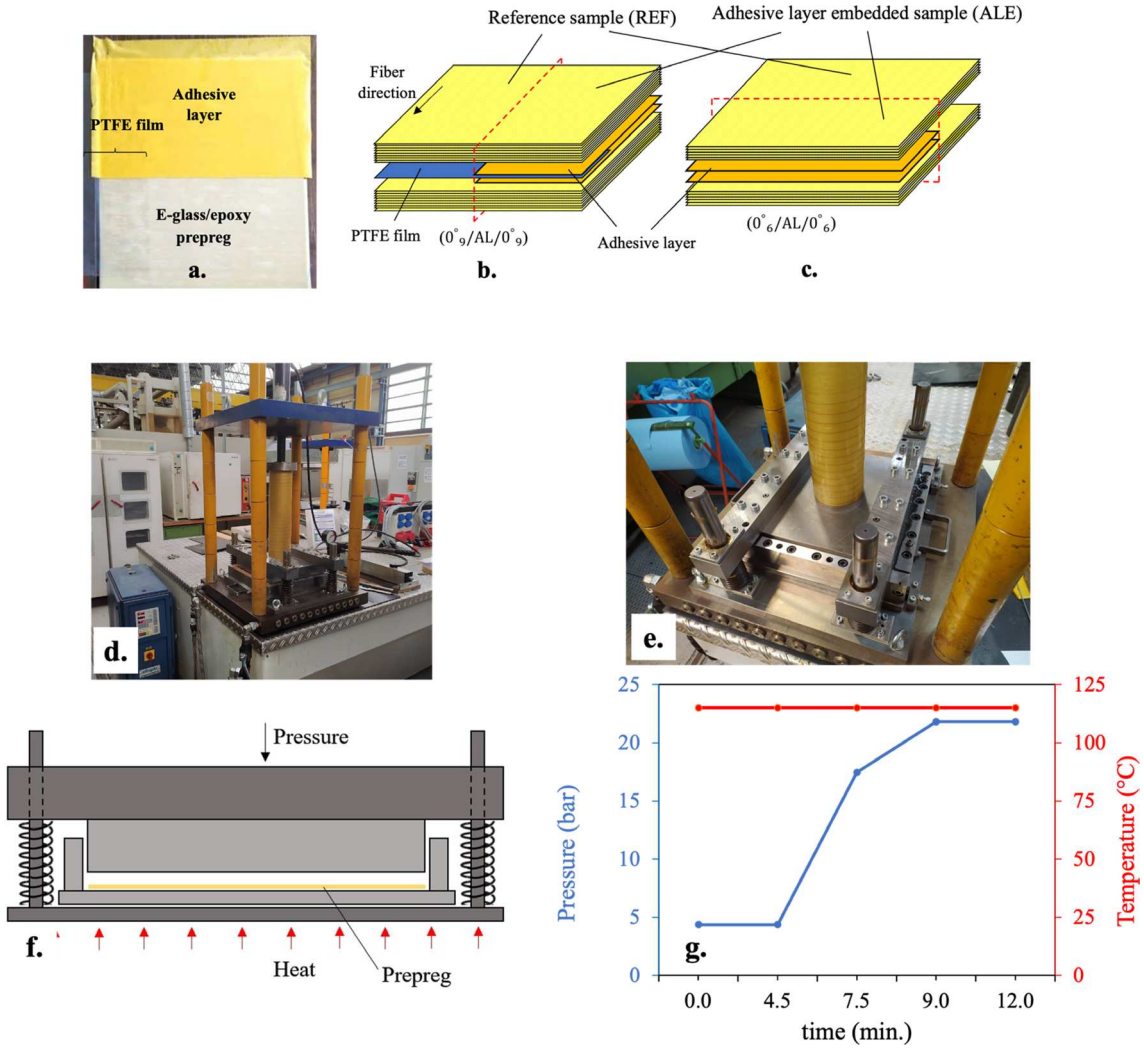

FIGURE 1 | Sample preparation with (a) placement of adhesive layer and PTFE film in laminate (top view), and laminate stacking sequences and schematics of adhesive layer position in half of composite sheets for (b) fracture sample and (c) tensile test sample, and sample manufacturing steps illustrating (d) hot press machine, (e) mold, (f) schematics of applied pressure and heat in mold, and (g) process parameters for pressure and temperature applied in hot press.

composite components (see Figure 1e,f). The process parameters for pressure and temperature, provided in Figure 1g, are applied during the curing process. Initially, the mold is heated to a steady-state temperature of 115°C. Once the temperature is stabilized, the laminated preform is inserted. An initial pressure of 4 bar is applied, followed by a gradual increase to 21.8 bar according to a specific profile. This pressure profile ensures void-free interlaminar bonding and an effective curing process. The bonding quality was evaluated through microscopy imaging and differential scanning calorimetry (DSC) analysis in the next sections. Then, the composite laminates are naturally cooled to room temperature under a constant pressure of 21.8 bar. After manufacturing, the sheets are tempered in an oven at 60°C for 6 h. The knitted fiber-reinforced adhesive films have possessed low thickness and high compliance, enabling them to conform effectively to the laminate layup without inducing significant distortion. Post-curing inspection has revealed no observable warping or unevenness, indicating that the interleaved films are well accommodated within the laminate architecture. The final thickness of the composite sheets is measured as 3.5 ± 0.03 mm for fracture test samples and 2.5 ± 0.02 mm for tensile test samples. Finally, test specimens are precisely cut from the manufactured composite plates using a waterjet system [68].

2.2 | Material Characterization and Mechanical Tests

2.2.1 | Optical Microscopy

The distribution of fibers and void content is examined following sample molding and surface polishing procedures, as outlined by Karimi et al. [12]. Optical microscopy images are captured using a Nikon LV100ND microscope at 100× magnification. Figure 2 presents cross-sectional micrographs of the REF and ALE samples, shown in Figure 2a,b, respectively. Both sample groups exhibit nearly uniform fiber distribution and interlaminar areas are free of voids, demonstrating the effectiveness of the manufacturing process. Figure 2c schematically illustrates the arrangement of glass fibers within the composite prepreg, highlighting the presence of midplane

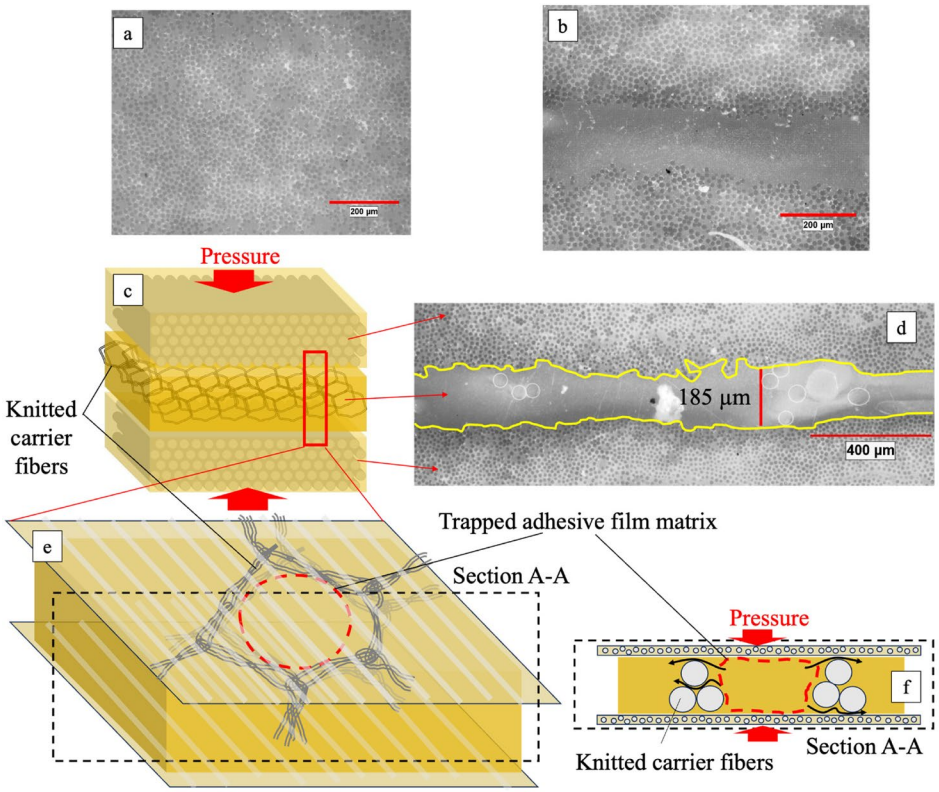

FIGURE 2 | Microscopic images of cross-sections showing (a) REF and (b) ALE samples; (c) a representative schematic of ALE samples; (d) variation in adhesive layer thickness and distribution of carrier fibers in ALE; (e) a magnified schematic representation of carrier fibers; and f. the role of carrier fibers in controlling adhesive layer thickness under pressure.

knit fibers embedded in the adhesive layer. These knit fibers act as a reinforcing mesh, providing structural support to the adhesive layer. Additionally, Figure 2d presents a wider cross-sectional micrograph of the ALE sample, where the sections of some carrier fibers within the adhesive film are marked. Notably, the adhesive layer exhibits thickness variations perpendicular to the fiber direction, potentially enhancing mechanical interlocking. The average adhesive layer thickness in this direction is measured at $185 \pm 50\,\mu m$ [69]. Furthermore, the cross-sectional micrograph reveals a void-free interface between the adhesive layer and the main composite matrix. This absence of voids, combined with the potential interlocking effect between the adhesive film and the composite matrix, suggests the likelihood of high interlaminar strength between these layers. Figure 2e,f, schematically depict the role of the knitted fibers in regulating the thickness of the adhesive layer by restricting the flow of the adhesive matrix under pressure during the manufacturing process. This restriction leads to the formation of a trapped adhesive film matrix between the carrier fibers, which play a crucial role during fracture. In the absence of the carrier fibers, the applied pressure in the hot press may induce excessive resin flow out of the mold, resulting in an excessively thin adhesive layer as the interleave.

Following mechanical testing, fractography, the fracture surfaces of the composite samples are examined using a Nikon SMZ800N Stereo Microscope. Further detailed analysis is conducted using a Zeiss 35VP field emission scanning electron microscope (FE-SEM) operated at an accelerating voltage of 3 kV, with images captured at various magnifications. To ensure sufficient electrical conductivity, the SEM specimens are coated with a thin layer of Fe prior to imaging.

Specifically, in this study, two layers of adhesive film are used to create a sufficiently thick interlayer matrix, maximizing toughening through the adhesive film. Understanding the role of the matrix in influencing the size of the plastic yield zone is crucial. An estimate of the plastic zone radius (r_y) for the matrix is determined based on experimental data, using Irwin's plastic zone model for plane strain, as reported by Ozdil and Carlsson [70], and is given by Equation (1):

$$r_y = \frac{1}{4\pi}\left(\frac{K_{IC}}{\sigma_y}\right)^2\left(\frac{3}{2}\left(1-2\upsilon^2\right)\right) \quad (1)$$

where K_{IC} is the critical stress intensity factor, which is directly related to the matrix's fracture toughness, σ_y denotes the tensile yield stress and υ is the Poisson's ratio of the matrix. Corresponding properties of the adhesive film epoxy obtained from the technical data sheet are listed in Table 1 [71].

Based on the values in Table 1, the interleave layer thickness, $2r_y$, is calculated to be $766.4\,\mu m$. This indicates that to achieve pure cohesive fracture using only the adhesive film matrix without the carrier knitted fibers, an interleave film thickness of $766.4\,\mu m$ would be required. For our samples, the adhesive film thickness before lamination is $190\,\mu m$, which is less than $2r_y$. This suggests that the fracture toughness of the interleave layer will continue to increase until it reaches $2r_y$, supporting

the validity of our approach to enhance fracture toughness by increasing the number of interlaminar adhesive films [72]. The presence of knitted fibers can restrict the plastic zone at the crack tip, potentially limiting the effectiveness of the adhesive film. However, on the other hand, the knitted fibers can also enhance fracture toughness by bridging the separation layers. These effects were thoroughly studied in this work.

2.2.2 | DSC Analysis

To investigate the suitability of the implemented pressure and temperature profile for both the prepreg and adhesive films, as well as to analyze the consistency between the adhesive layer matrix and the main prepreg matrix, DSC analysis is carried out using a NETZSCH STA 449F3 device. The analyses are conducted in the temperature range of 25°C–250°C with three cycles (heating–cooling–heating) at a rate of 5°C/min.

The DSC diagram for the second heating cycle is depicted in Figure S1. No exothermic peak is observed, indicating successful curing of the epoxy for both materials. The measured glass transition temperatures (T_g) are 112.3°C and 110.3°C for the cured prepreg material and cured adhesive layer, respectively. The T_g values of the primary epoxy matrix and the interleaved film resin are found to be closely matched. This similarity, in conjunction with their shared epoxy-based chemistry, suggests a degree of thermal and phase compatibility. Such alignment reduces the likelihood of thermal mismatch stresses and phase separation during curing or in service, thereby supporting cohesive integration of the interleaf within the laminate system [60]. A small drop in the adhesive layer's DSC diagram is observed around 220°C, which is attributed to the melting of minor toughening additives within the adhesive layer. This phenomenon does not affect the overall manufacturing process. Additionally, the DSC diagrams confirm that the applied temperature of 115°C during the manufacturing process is sufficient to fully complete the curing process within the hot press.

2.2.3 | Mechanical Tests

To investigate the effect of the adhesive layer on both in-plane and fracture toughness properties, three types of mechanical tests are performed: transverse tensile tests, Mode-I fracture tests, and Mode-II fracture tests.

Transverse tensile tests are conducted on REF and ALE samples to assess the effect of adhesive layers on in-plane properties while suppressing the dominance of fiber tensile strength. Samples with dimensions of 175 mm × 25 mm and an average thickness of 2.5 mm are cut from composite laminates. Aluminum tables (25 mm × 25 mm) are bonded to the ends of the samples. An Instron machine with a 100 kN capacity is used to perform the tests in accordance with the ASTM D3039 standard, from which stress–strain curves are obtained [67].

To quantify interlaminar fracture toughness, DCB tests are used to measure Mode-I fracture toughness, and edge notch flexure (ENF) tests are used to assess Mode-II fracture toughness. These tests are conducted in accordance with ASTM D5528 [65] and ASTM D7905 [66] standards, respectively.

For Mode-I fracture tests, three samples are prepared for each group, and two hinges are bonded to the pre-cracked end of each sample (Figure S2a). To facilitate the monitoring of crack propagation, the cross-section of each sample was painted white and marked with vertical lines at 1 mm intervals for the first 5 mm, followed by 5 mm intervals beyond the pre-crack tip. Tests are performed at a constant displacement rate of 2 mm/min. Crack propagation distance, applied force, and crack opening displacement are continuously monitored and recorded in real-time using the Instron test machine (Figure S2b). Load versus crack opening displacement and strain energy release rate versus crack propagation diagrams are generated. The Mode-I critical strain energy release rate (G_{IC}) is calculated using the modified beam theory specified in ASTM D5528 (Equation 2):

$$G_{IC} = \frac{3P\delta}{2b(a + |\Delta|)} \tag{2}$$

where P (N) is the applied load, δ (mm) is the load point displacement, b (mm) is the sample width, a (mm) is the crack length, from the loading point to the crack tip, and Δ (mm) is the correction factor. The maximum load is considered the crack initiation point, and the calculation is performed individually for the crack initiation and propagation phases.

During the ENF tests, the compliance-calibration (CC) approach is used to determine the Mode-II critical strain energy release rate (G_{IIC}). Initial tests with crack lengths of 20 mm and 40 mm are conducted to establish the correlation between sample compliance (C) and the cubic function of crack length (a^3) with compliance markers are positioned at $a = 20$, 30, and 40 mm from the PTFE layer tip (Figure S2c). Tests are conducted at a crosshead loading rate of 0.5 mm/min using the Instron set-up (Figure S2d). The compliance-calibration coefficients A and m are determined through least squares regression analysis, establishing the relationship, $C = A + ma^3$. Then, G_{IIC} is calculated using Equation (3):

$$G_{IIC} = \frac{3P^2ma_0^2}{2b} \tag{3}$$

where P is the applied load (N), m is a constant value from the regression analysis, a_0 is the initial crack length (mm), and b is the sample width (mm). Similarly, three samples are tested for each REF and ALE groups. The G_{IIC} value only was calculated for crack initiation not for propagation.

3 | Results and Discussion

This section presents the results of the mechanical tests followed by the fractography to elucidate the failure mechanisms in correlation with the mechanical tests.

3.1 | Transverse Tensile Test Results

In this study, transverse tensile tests are conducted with fibers oriented perpendicular to the loading direction to evaluate the effect of the adhesive layer on the in-plane performance

of composites. Transverse tensile tests were conducted to assess the influence of the interleaved adhesive film on matrix-dominated mechanical behavior [73]. As the reinforcement fibers within the interleaf are not aligned with the laminate's primary fiber direction, their effect on longitudinal mechanical performance is minimal. Thus, evaluating the E_{22} modulus provides a more representative measure of the structural interaction between the interleaved film and the laminate. Table 2 lists the Young's modulus, Poisson's ratio, and tensile strength for both reference (REF) and adhesive layer-embedded (ALE) samples. Figure S3 illustrates the stress–strain diagrams obtained from the transverse tensile tests for both sample types. As expected, the ALE samples exhibit lower Young's modulus and tensile strength under tensile loading perpendicular to the fiber direction. Specifically, the ALE samples show a 20.82% reduction in Young's modulus and a 7.63% reduction in tensile strength compared to the REF samples. The reduction in tensile strength is attributed to the fiber-matrix interfaces of the knit fibers embedded in the adhesive layer, which act as stress concentration points. Additionally, since some of these fibers in the adhesive layer are not aligned with the tensile force, breakage initiates in the adhesive layer under high-stress conditions. The reduction in E_{22} observed in the ALE samples is attributed to local compliance induced by the knitted fiber architecture and resin-rich zones within the interleaved film. These knitted regions, while beneficial for fracture toughness, disrupt continuous load transfer paths in the transverse direction. This disruption leads to localized strain accumulation and reduces the effective stiffness. While stress concentrations typically affect strength, their influence on local compliance can indirectly contribute to a decrease in the measured transverse modulus. Further discussion will be provided through detailed fractographic analysis of the fracture surfaces in Section 3.4.

Building on the matrix-dominated failure mechanisms discussed earlier, both REF and ALE samples exhibit very low Poisson's ratios, with the ALE samples showing even lower values. When fibers are oriented perpendicular to the loading direction, their contribution to load-bearing is negligible, leaving deformation behavior predominantly controlled by the epoxy matrix. The epoxy matrix, with its significantly lower stiffness compared to the fibers, undergoes axial stretching under tensile loading. However, the transverse fibers—particularly in the ALE samples, where the adhesive layer's knit fibers further restrict lateral movement—severely limit transverse contraction. This constraint results in minimal lateral strain, thereby producing the observed low Poisson's ratios. These findings align with the earlier observation of reduced stiffness and strength in ALE samples, underscoring the critical role of matrix-adhesive interactions in governing deformation behavior.

TABLE 2 | In-plane properties of REF and ALE samples under transverse tensile test.

Sample	Young's modulus (E22) (GPa)	Poisson's ratio ($\nu_{12} = \nu_{13}$)	Tensile strength (MPa)
REF	10.7 ± 0.29	0.069 ± 0.004	61.2 ± 10.35
ALE	8.4 ± 0.20	0.062 ± 0.002	56.5 ± 3.02

3.2 | Mode-I Fracture Test Results

The DCB tests are conducted following the methodology outlined in Section 2.2, with G_{IC} values calculated using Equation (2). Figure 3 presents load-crack opening displacement diagrams and R-curves for a representative REF sample and all ALE samples. Table 3 presents the average G_{IC} values with standard deviations in both crack initiation and crack propagation phases. From the force-displacement curves, for ALE samples, the force initially rises before decreasing as the crack propagates, whereas the REF samples exhibit a simpler force reduction profile. (Figure 3a). Only one of the REF samples is presented as a representative diagram in Figure 3a. Moreover, during the Mode I tests, ALE samples demonstrated larger C= (COD) compared to REF samples. This is primarily due to the presence of knitted fibers within the interleaved zone, which engage in energy-dissipating mechanisms such as fiber bridging and pull-out. These mechanisms contribute to a more gradual and stable crack propagation, resulting in a larger area under the load–COD curve and indicating a more ductile fracture behavior. Representative load–COD curves are shown in Figure 3a. Before reaching the peak load, ALE samples exhibit varying slopes, indicating differences in effective stiffness. This variation can be attributed to differences in the fracture mechanisms occurring immediately beyond the crack tip during crack initiation. This variation in crack initiation behavior is attributed to the presence of the adhesive film at the crack tip, which influences the local fracture mechanism. Considering the maximum force as the crack initiation criterion, Figure 3b shows the G_{IC} versus crack length for the REF sample, with the linear R-curve indicating stable crack propagation (maximum standard deviation value of 0.028 kJ/m^2). In contrast, all three ALE samples have displayed distinct fracture behaviors. While fracture forces in ALE samples are consistently higher than those of the REF sample, their load–displacement curves have exhibited significant fluctuations and unstable crack growth. This stick–slip propagation which is characterized by abrupt force drops, is commonly observed in DCB testing of ductile matrix composites [49, 50, 74, 75]. The instability is attributed to localized variations in fracture mechanisms, resulting in a high standard deviation of G_{IC}.

The maximum load-bearing capacity of the REF samples is 47.3 N, while the average value for ALE samples reaches 100.5 N, representing a 112.5% increase. For crack initiation, ALE samples exhibit a G_{IC} of 2.3 kJ/m^2, a 365.39% improvement over REF samples (0.5 kJ/m^2). This suggests that the adhesive layer significantly enhances Mode-I fracture toughness during initiation by absorbing elastic energy and delaying crack propagation. However, as the crack advances, G_{IC} values exhibit considerable fluctuations and unstable growth, reflected in a high standard deviation (0.5 kJ/m^2) during propagation (Figure 3c and Table 3). The average fracture toughness of ALE samples remains significantly higher than REF samples, with 175.47% improvement in propagation, though toughness declines sharply beyond 40 mm of crack growth. This instability arises from competing mechanisms: the adhesive layer initially resists crack propagation through energy absorption but accelerates it in weaker regions due to localized stress concentrations. The 2-layer adhesive film demonstrates optimal effectiveness within the first 40 mm of propagation, after which toughness drops

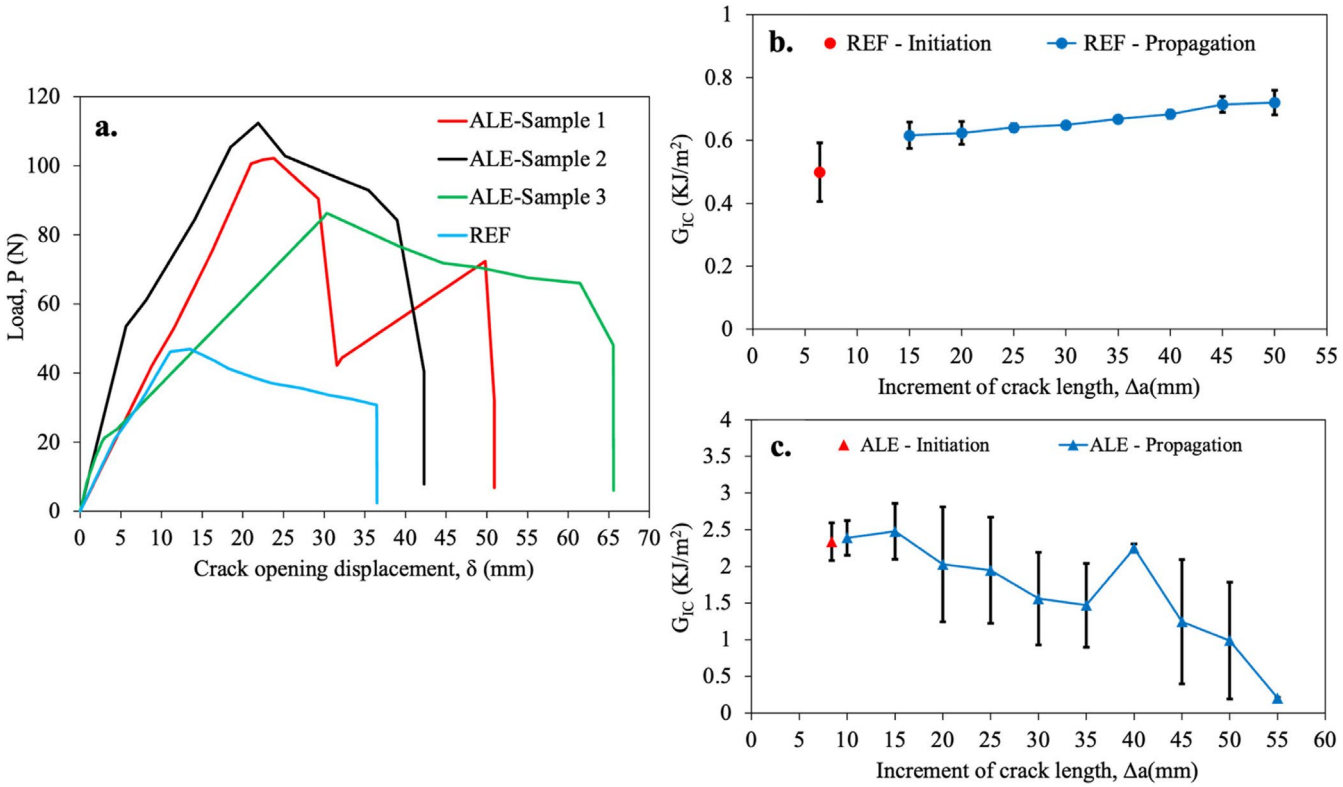

FIGURE 3 | (a) Load–displacement curves, and G_{IC}—crack length diagrams of DCB samples for (b) REF and (c) ALE samples.

TABLE 3 | G_{IC} values for crack initiation and propagation.

Sample	$G_{IC\_initiation}$	$G_{IC\_propagation}$
REF	0.50 ± 0.09	0.60 ± 0.003
ALE	2.33 ± 0.26	1.65 ± 0.50
Increment	365.39%	175.47%

significantly. The significant variation in fracture forces and G_{IC} standard deviations, are attributed to shifting fracture mechanisms along the crack path, will be analyzed in detail in the fractography section, focusing on adhesive-matrix interactions and failure modes.

3.3 | Mode-II Fracture Test Results

Mode-II fracture tests are conducted in accordance with the ASTM D7905 standard, which excludes crack propagation monitoring. Figure 4a presents the representative load-flexural displacement curves for ENF samples, with the maximum bearing load annotated for each curve. The ALE samples exhibit a maximum load of 1019 N, representing a 37.88% improvement over REF samples (739 N). This significant increase in load-bearing capacity underscores the enhanced resistance to crack initiation in Mode-II loading.

Figure 4b shows the calculated G_{IIC} values for REF and ALE samples, determined using the compliance-calibration method described in Section 2.2.3. The REF samples showed a G_{IIC} value of $2.11 \pm 0.67\,kJ/m^2$, whereas the ALE samples achieve a G_{IIC} value of $5.73 + 1.7\,kJ/m^2$, reflecting a 171.5% improvement compared to REF samples. This dramatic increase is attributed to the adhesive layer's ability to absorb strain energy under Mode-II fracture, thereby significantly enhancing delamination resistance.

3.4 | Fractography

3.4.1 | Transverse Tensile Fractography

The fracture surfaces of transverse tensile test samples were analyzed using SEM to elucidate the mechanisms underlying the mechanical behavior observed in Section 3.1. Figure 5 compares the fracture surfaces of REF and ALE samples, with key features correlated to the reduction in Young's modulus, tensile strength and Poisson's ratio reported in Table 2.

The fracture surface of the REF sample exhibits fiber breakage, matrix cracking, and separation of fiber bundles from the epoxy matrix (Figure 5a). Residual matrix adhering to the fibers confirms strong interfacial bonding, consistent with the REF sample's higher tensile strength (61.2 ± 10.35 MPa) and Young's modulus (10.7 ± 0.29 GPa). These results align with the uniform fiber distribution and void-free microstructure observed in Figure 2a. This observation remains consistent for the ALE samples as depicted in Figure 5b. However, in ALE samples, stress concentrations at the interfaces between the adhesive layer's knit fibers and the surrounding matrix initiate failure. Scarps and river lines (Figure 5b) mark crack initiation sites, while fiber pullout within the adhesive layer creates voids and holes (Figure 5c). These mechanisms explain the deterioration in the in-plane mechanical performance

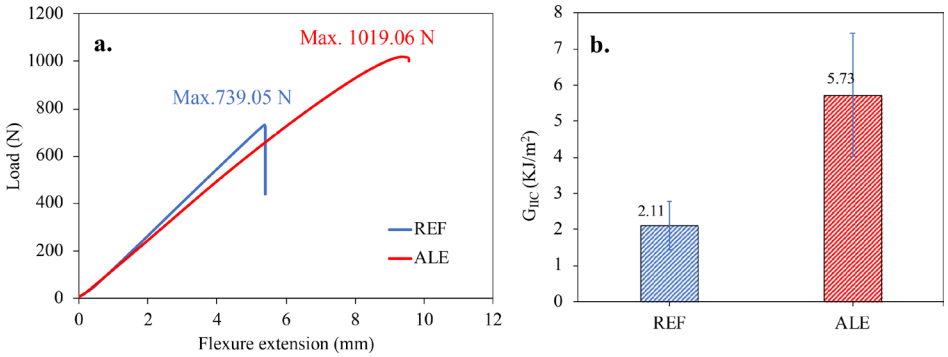

FIGURE 4 | (a) Load-flexure extension and (b) G_{IIC} diagrams of ENF samples for REF and ALE samples.

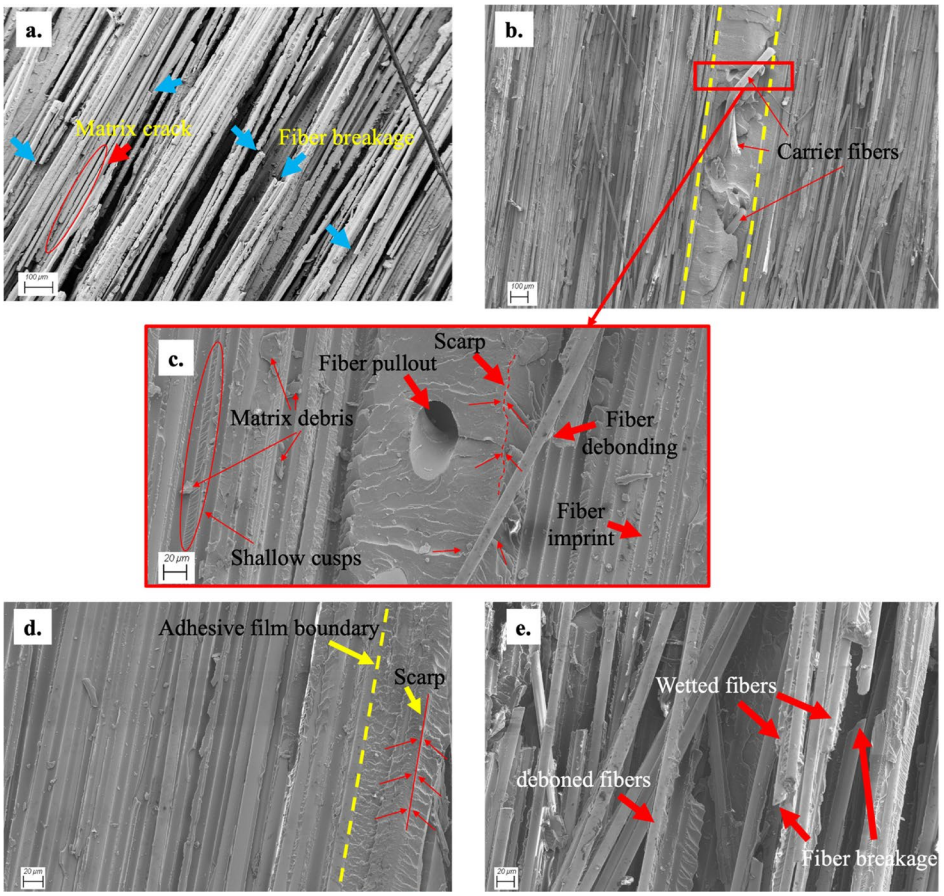

FIGURE 5 | SEM image of fracture surface after transverse tensile test for (a) REF and (b–e) ALE samples.

of ALE samples in comparison to REF samples, as highlighted in Table 2. Brittle matrix failure, evidenced by residual matrix fragments, correlates with the low Poisson's ratios, as transverse fiber constraints suppress lateral contraction.

Moreover, the adhesive layer forms a void-free interface with the primary matrix (Figure 5d), confirming effective bonding. However, shear traces and scarps on the adhesive layer highlight localized stress redistribution, consistent with unstable crack growth and fluctuations in the stress–strain curves. Residual primary matrix on fibers (Figure 5e) reaffirms strong fiber-matrix adhesion, though misaligned knit fibers in the adhesive layer act as weak points, promoting premature failure.

3.4.2 | Mode-I Fractography

Figure 6 presents microscopy and SEM images of fracture surfaces from Mode-I DCB tests on the reference (REF) sample. Figure 6a highlights fiber bridging ahead of the crack tip, a key toughening mechanism for reference samples. Figure 6b reveals randomly oriented broken fibers, indicative of fiber pull-out and bridging phenomena. The representative SEM image in Figure 6c confirms robust fiber-epoxy adhesion, evidenced by fiber breakage and pullout, while Figure 6d shows micro-dimples in the epoxy matrix, indicative of plastic deformation and ductile fracture behavior [48]. Figure 6e schematically illustrates the crack path, which oscillates between the primary matrix and fiber-matrix interface. This alternating path

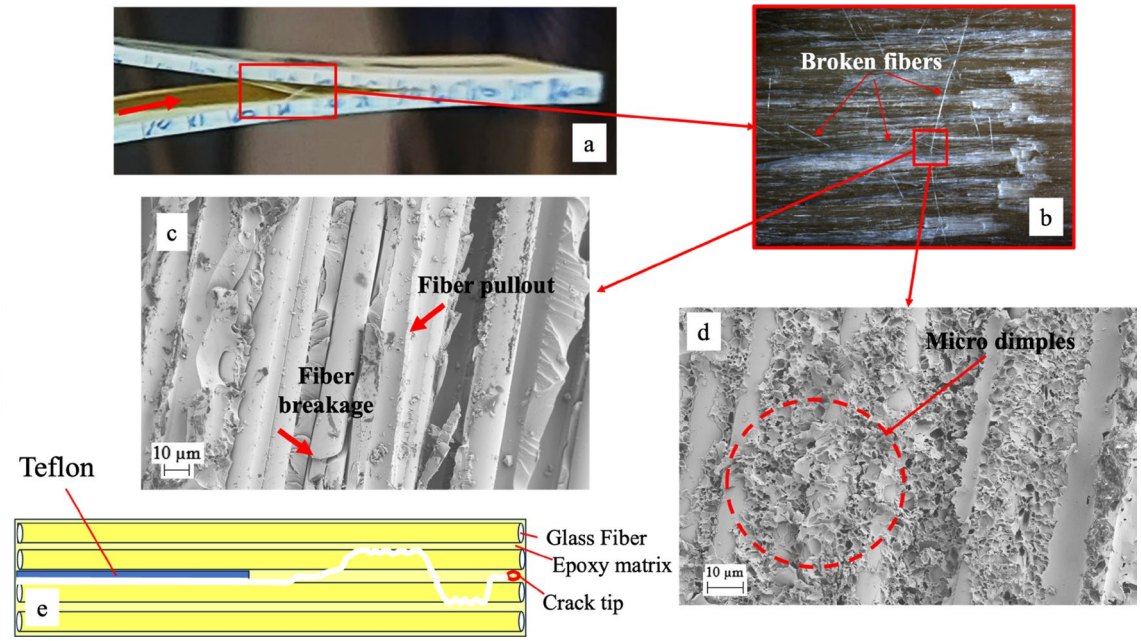

FIGURE 6 | Fractography of REF sample under Mode-I test.

activates toughening mechanisms—fiber bridging, pullout, and matrix plasticity—consistent with findings in ductile composite systems [7, 31, 75, 76]. These mechanisms correlate with the rising R-curve observed in REF samples (Figure 3b), where the G_{IC} increases during propagation due to progressive energy dissipation. The trend stabilizes at steady-state crack growth, dominated by sustained fiber bridging. Thus, this fractographic analysis aligns with the mechanical results: while REF samples exhibit lower G_{IC} values compared to ALE samples (Table 3), their stable propagation and rising toughness underscore the effectiveness of intrinsic toughening mechanisms in noninterleaved composites.

Figure 7 explores the relationship between crack propagation and applied load by correlating load-crack length curves (from Figure 3a,c) with fracture surface images for three ALE samples. Each sample is analyzed in paired panels: ALE sample 1 (Figure 7a,b), ALE sample 2 (Figure 7c,d), and ALE sample 3 (Figure 7e,f). Distinct whitish and yellowish regions on the fracture surfaces (Figure 8b,d,f) demarcate shifts in fracture mechanisms, with dashed lines indicating the onset of color transitions and corresponding load drops.

Using Equation (2) and experimental data from Figure 3c, the G_{IC} values are calculated with the lengths of these areas are quantified and juxtaposed with the crack propagation length in the diagrams for all REF and ALE samples. Figure 8 presents the average G_{IC} values for the REF sample and three ALE samples where for ALE samples the corresponding values for the whitish and yellowish areas as Area A and Area B, respectively. The location and length of the whitish and yellowish areas in Figure 7b,d,f exhibit randomness, which contributes to the variation in the reported G_{IC} values for the two distinct fracture surface colors of the ALE samples in Figure 9. The inclusion of the adhesive layer significantly increases the G_{IC} values compared to the REF samples. Notably, cracks within the whitish areas demonstrate higher G_{IC} values for propagation compared to those in the yellowish areas. Moreover, based on force-time data observations for ALE samples during the experimentation it is evident that cracks in the white area propagate at a slower pace compared to other areas, owing to a higher strain energy absorption during crack propagation. These findings underscore the adhesive layer's dual role: improving initiation toughness through energy dissipation while introducing instability via interfacial weaknesses.

To investigate the fracture mechanisms underlying the distinct whitish and yellowish regions observed during Mode-I testing, a detailed microscopic analysis of ALE samples is conducted (Figure 9). Figure 9a depicts the fracture surface of ALE sample 2, highlighting the whitish and yellowish regions. Three primary failure modes are identified: (1) adhesive failure, characterized by complete separation of the adhesive layer from the primary matrix due to weak interfacial bonding (Figure 9b); (2) thin-layer cohesive failure, where partial adhesive separation and knit fiber remnants create tortuous, zigzag crack paths that enhance fracture toughness through significant strain energy absorption (Figure 9c); and (3) midplane cohesive failure, involving crack propagation along the adhesive layer's midplane, resulting in pulled-out knit fibers and smooth fiber-matrix interfaces indicative of weak bonding (Figure 9d) [77]. Whitish regions, dominated by thin-layer cohesive failure, exhibit slow crack growth and stable G_{IC} values (2.33 kJ/m^2), correlating with high-energy absorption. In contrast, yellowish regions, governed by midplane cohesive failure, show rapid propagation along weak interfaces, leading to erratic G_{IC} fluctuations (standard deviation: 0.5 kJ/m^2, Figure 3c) and declining toughness beyond 40 mm crack length. The transition between these mechanisms explains the fluctuating R-curves (Figure 7) and high standard deviations, driven by competing energy dissipation (tortuous paths in whitish areas) and interfacial weaknesses (midplane failure in yellowish areas).

In order to correlate the fracture mechanisms on the micro level and validate the findings from the microscopy study

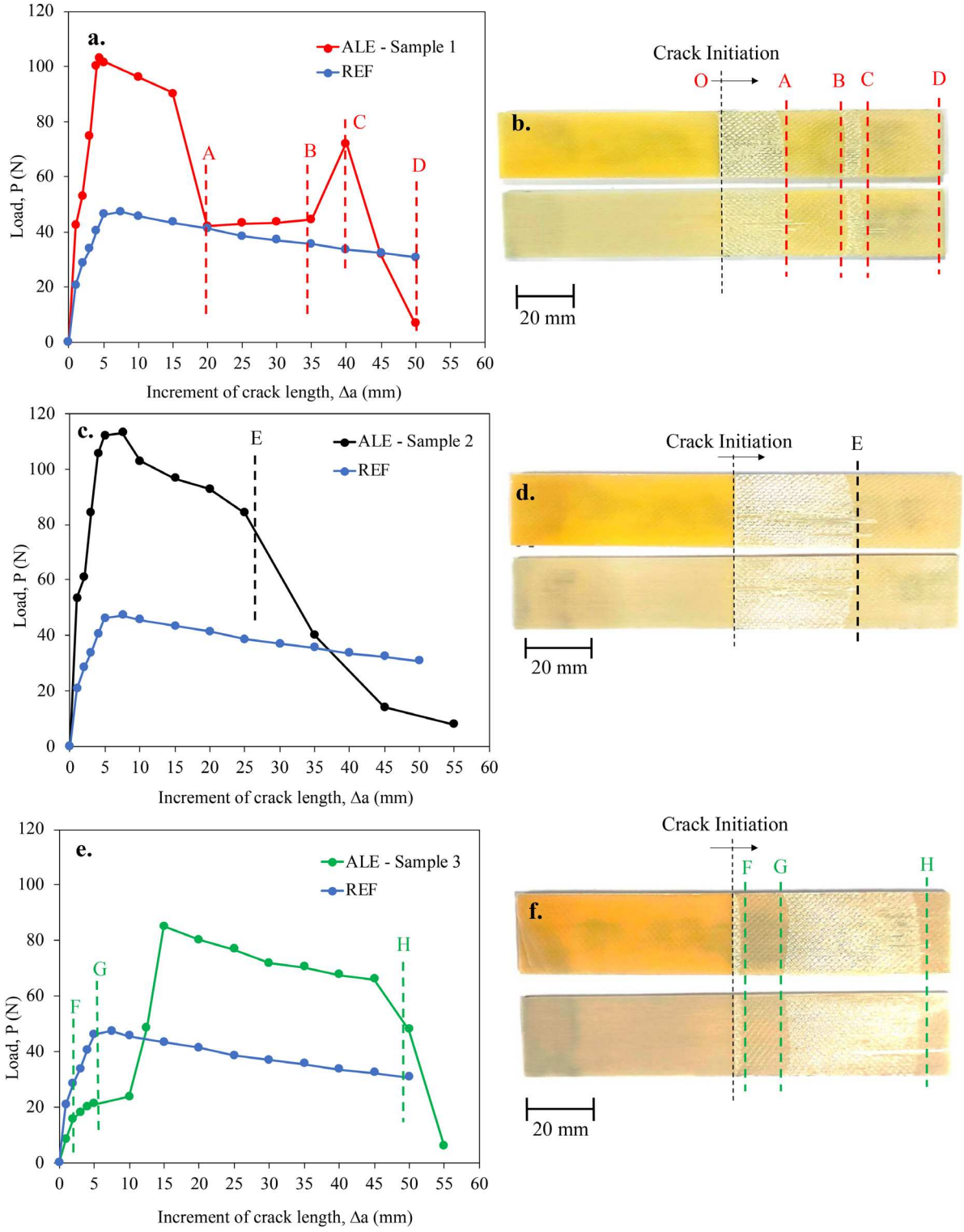

FIGURE 7 | Correlation between load-crack length curves (a, c, and e) and fracture surface images (b, d, and f) for ALE samples 1, 2, and 3, respectively under Mode-I fracture tests.

presented in Figure 9, scanning electron microscopy (SEM) imaging is conducted on two distinct areas of the fracture surface obtained from Mode-I fracture tests. Figure 10 presents a schematic for the crack propagation path based on fractography through SEM images. In the initiation of a crack at the tip of the Teflon film, the crack propagates toward one of bending arms creating a trapezius trace of shear effect on adhesive film matrix, as illustrated in Figure 10a. Fiber imprints are visible, indicating poor adhesion between the knit fibers of the adhesive film and the composite matrix, as well as bridging phenomenon. Subsequently, the crack follows a zigzag trajectory through the adhesive layer, alternating its propagation direction between the upper and lower interfaces of the adhesive-main matrix, as depicted in the two microcopy images taken from adjacent regions Figure 10b1. In certain areas, the crack propagates along the boundary between the adhesive film and

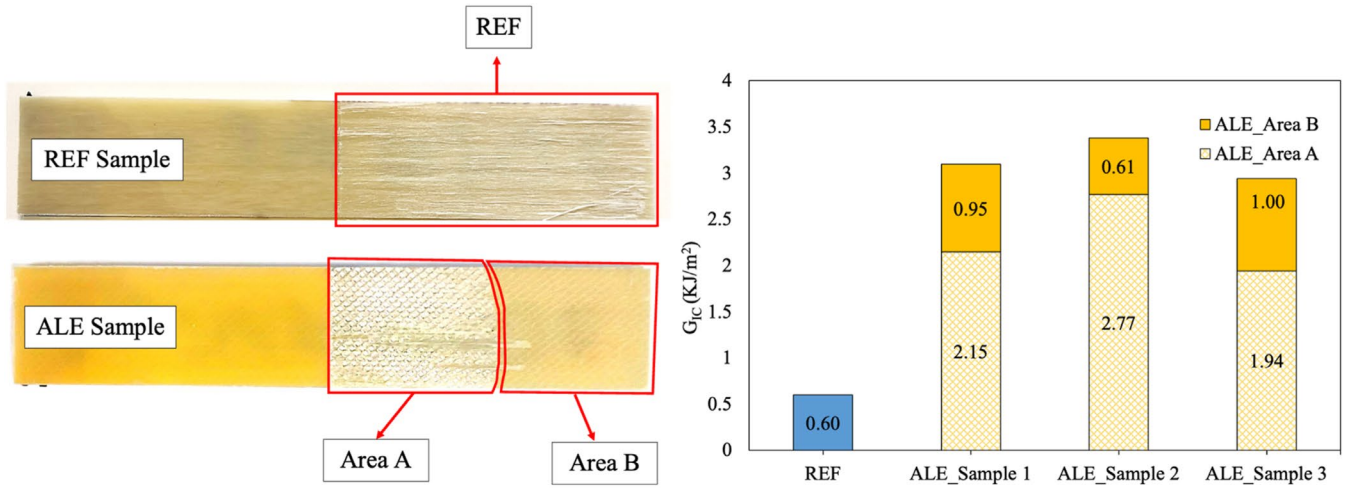

FIGURE 8 | Representative fracture surfaces and G_{IC} values of the REF and three ALE samples with portions of area A (whitish) and area B (yellowish).

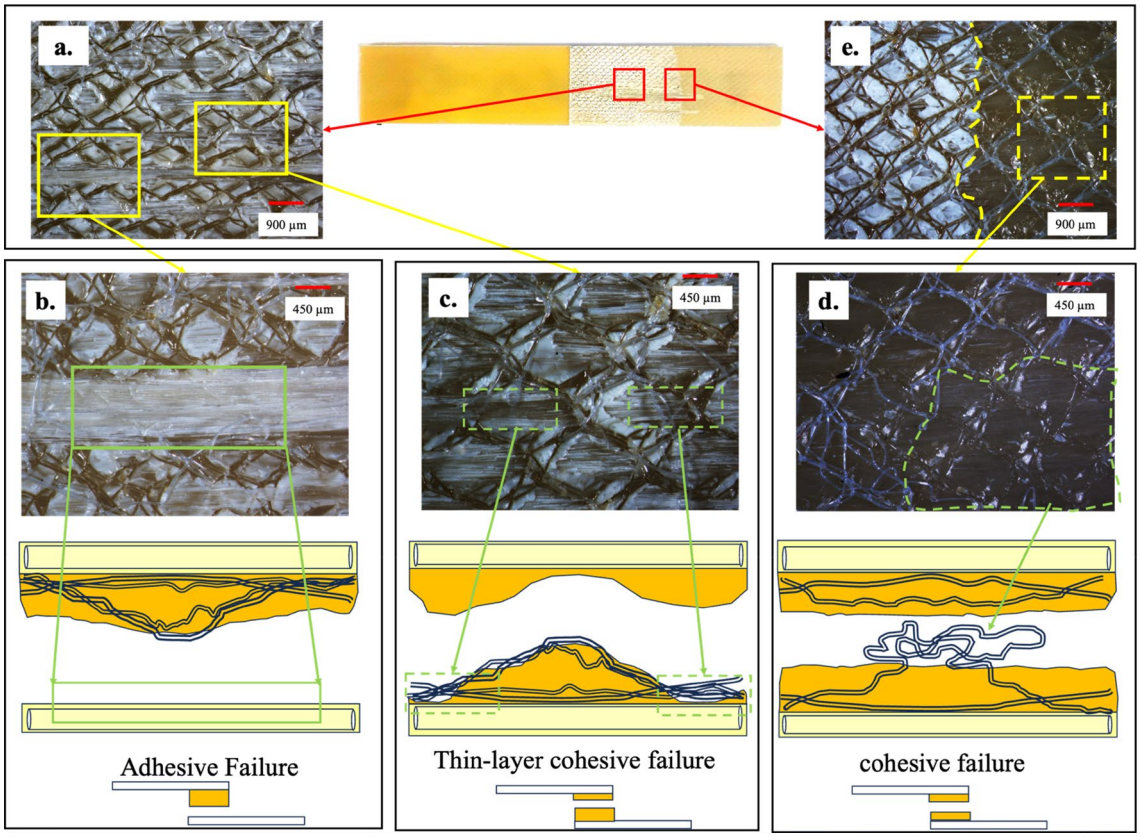

FIGURE 9 | Stereo-microscopy images and attributed fracture mechanisms for DCB samples under Mode-I fracture tests for ALE samples exemplifying for (a) ALE sample 2, (b) whitish region with adhesive failure and (c) thin-layer cohesive failure: and for yellowish region (d) cohesive failure mechanisms and (e) boundary between two distinct fracture areas.

the main matrix, detaching the adhesive matrix and exposing the underlying glass fibers, as shown in Figure 10b2. The schematics with two layers adhesive film illustrates how the presence of knit fibers influences the deviation of the crack tip and leads to the formation of shear traces in multiple directions. This is depicted in Figure 10c, where colored vectors represent the directions of the shear forces. Furthermore, the pocket of resin in Figure 10c originates from the adhesive layer epoxy, which is expected to provide a sufficient matrix for plastic deformation and ductile fracture behavior, resulting in a significant enhancement in energy dissipation. These phenomena promote a tortuous crack path, leading to high strain energy absorption during propagation and an improvement in the G_{IC} value. In the previously illustrated fractures in Figure 9b,c, adhesive failure and thin-layer cohesive failures happen through this phase of crack propagation. The dashed

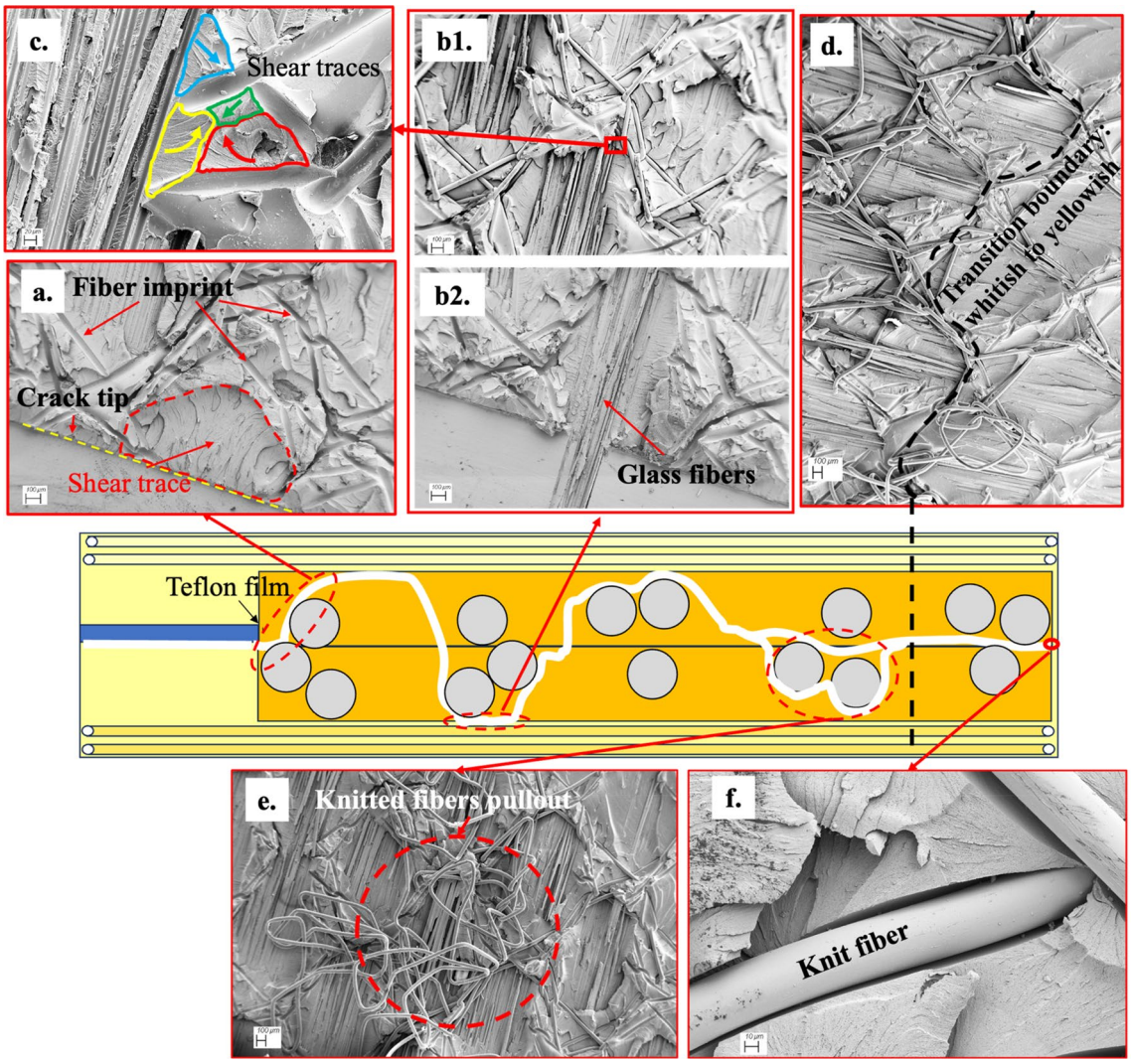

FIGURE 10 | Schematic representation of crack path and SEM images of the fracture phases for ALE sample under Mode-I test.

line in Figure 10d marks the boundary where the crack transitions into the mid-plane of the adhesive layer. This transition is indicated by a color change on the fracture surface, from whitish to yellowish regions, signifying a shift from thin-layer cohesive failure to cohesive failure, as shown in Figure 9e. At the adhesive layer interface, the crack pulls out the knit fibers, creating a bulk of fibers at the interface, as shown in Figure 10e. During inspection using both microscopy and SEM imaging, broken knitted carrier fibers were rarely observed. This indicates that the knitted fibers generally maintain their integrity. In most cases, clusters of distorted knitted fibers were evident on the fracture surfaces especially when crack propagates into midplane region. In the cohesive failure area, the knit fibers are deboned from the adhesive layer matrix, exhibiting a very smooth fiber surface without any resin residue, as seen in Figure 10f. This lack of visible damage to the fibers suggests poor interfacial bonding between the carrier fibers and adhesive matrix. From Figure 10, it can be concluded that the carrier fibers provided a bridging effect and induced crack tip deviation, serving as toughening mechanisms. However, they themselves played a significant role in random shifting between different fracture mechanisms under Mode-I loading as illustrated in Figure 9. The crack propagation in midplane of two adhesive films limits the effectiveness of adhesive film matrix which could otherwise enhance toughness by providing increased plastic deformation.

In summary, the toughening mechanisms observed in Mode-I fracture of the adhesive layer include fiber pull-out, fiber bridging, fiber breakage, and plastic deformation of the adhesive layer matrix. These mechanisms contribute to the elevation of the R-curves, as depicted in Figure 3a. However, crack propagation along with declining G_{IC} values and high standard deviation, in Figure 3c, all were attributed to the transition in crack propagation characteristics from thin-layer cohesive failure to cohesive failure between the adhesive layers. In fact, the weak bonding between carrier fibers and adhesive film matrix facilitated a growth surface for crack propagation in this region.

To investigate the factors governing random crack patterns and color variations in fracture surfaces, through-thickness microscopy analysis was conducted on ALE sample 1 (Figure 7b), which exhibited multiple transitions between thin-layer cohesive failure (whitish regions) and midplane cohesive failure (yellowish regions). Figure 11a shows microscopy images of

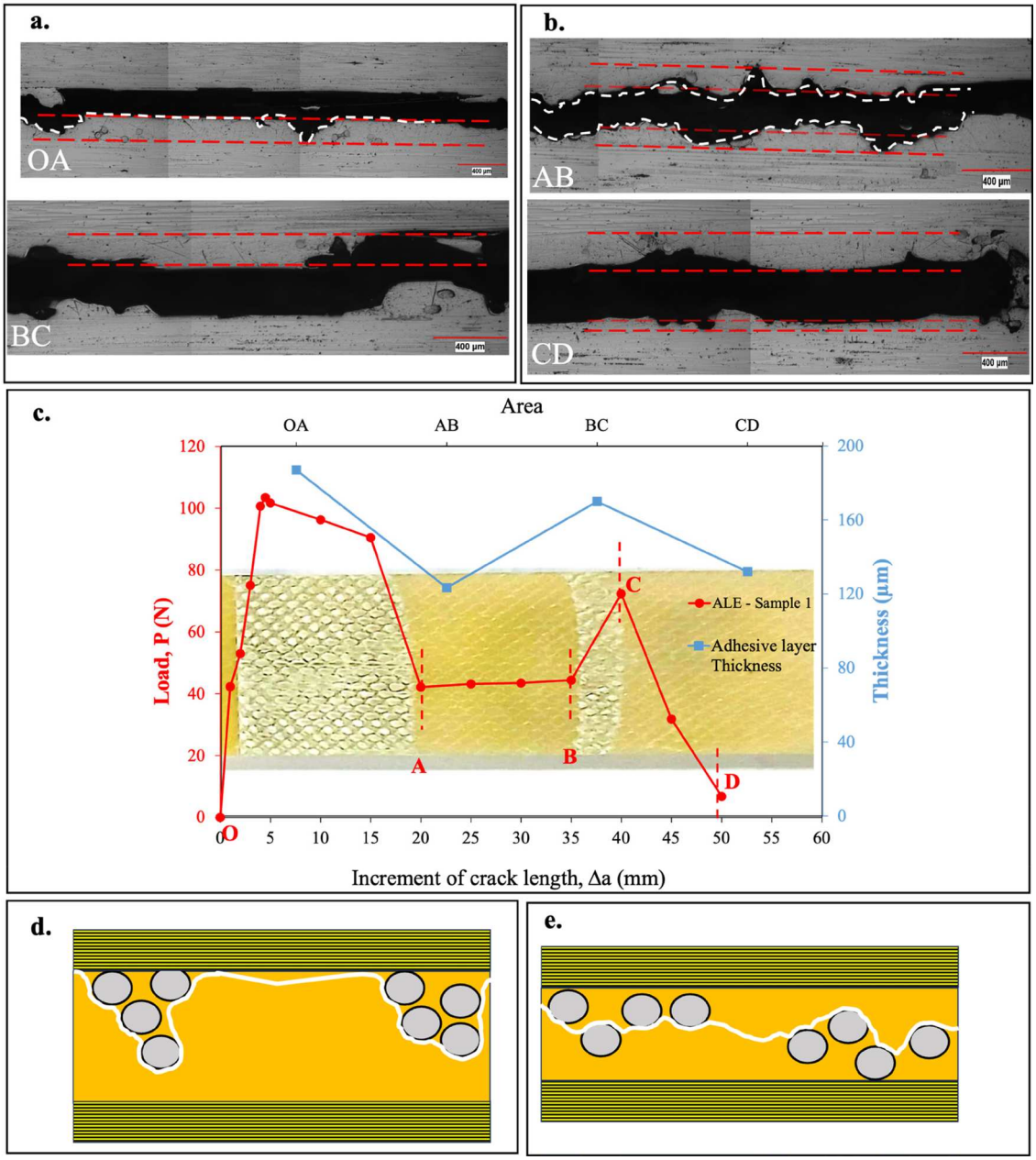

FIGURE 11 | Correlation between fracture mechanism and carrier fibers positioning. Cross-sectional microscopy images represent (a) thin-layer cohesive failure, (b) cohesive failure, (c) load and thickness variation curves with crack length, and schematic representation of crack growth and thickness variation for (d) thin-layer cohesive failure, and (e) cohesive failure.

the sections for top and bottom fracture surfaces for the OA and BC regions, illustrating thin-layer cohesive failure with adhesive layer residuals visible at the bottom and top, respectively. Figure 11b represents the fracture surfaces for regions AB and CD (Figure 7b) with pure cohesive failure, marked by yellowish fracture surfaces. The dashed lines in Figure 12a,b indicate the distances used for measuring the adhesive layer thickness across all four regions: OA, BC, AB, and CD. Based on microscopy images, the presence of adhesive layer residuals on both the top and bottom layers indicates pure cohesive type failure. The average adhesive film thickness was measured as 187 and 170 μm for regions OA and BC, respectively, while for regions AB and CD, the average thickness was 123.5 and 132 μm, respectively. These measurements are then plotted against the increment of crack length in the same plot alongside corresponding load data, as depicted in Figure 11c. Based on the microscopy images (Figure 11a,b), the crack surface profile, indicated by the white dashed line, shows that the distribution and positioning of the knitted carrier fibers play a significant role in determining the fracture mechanism.

Clustered carrier fibers in OA and BC regions create resin-rich zones, forcing cracks into thin-layer cohesive paths that due to the strong bonding between the adhesive film matrix and the main matrix, dissipate significant energy (schematic in Figure 11d). Conversely, evenly distributed fibers in thinner regions (AB, CD) promote weak midplane interfaces, enabling rapid propagation with minimal energy dissipation (schematic in Figure 11e), consistent with declining G_{IC} values and high standard deviations (Figure 3c).

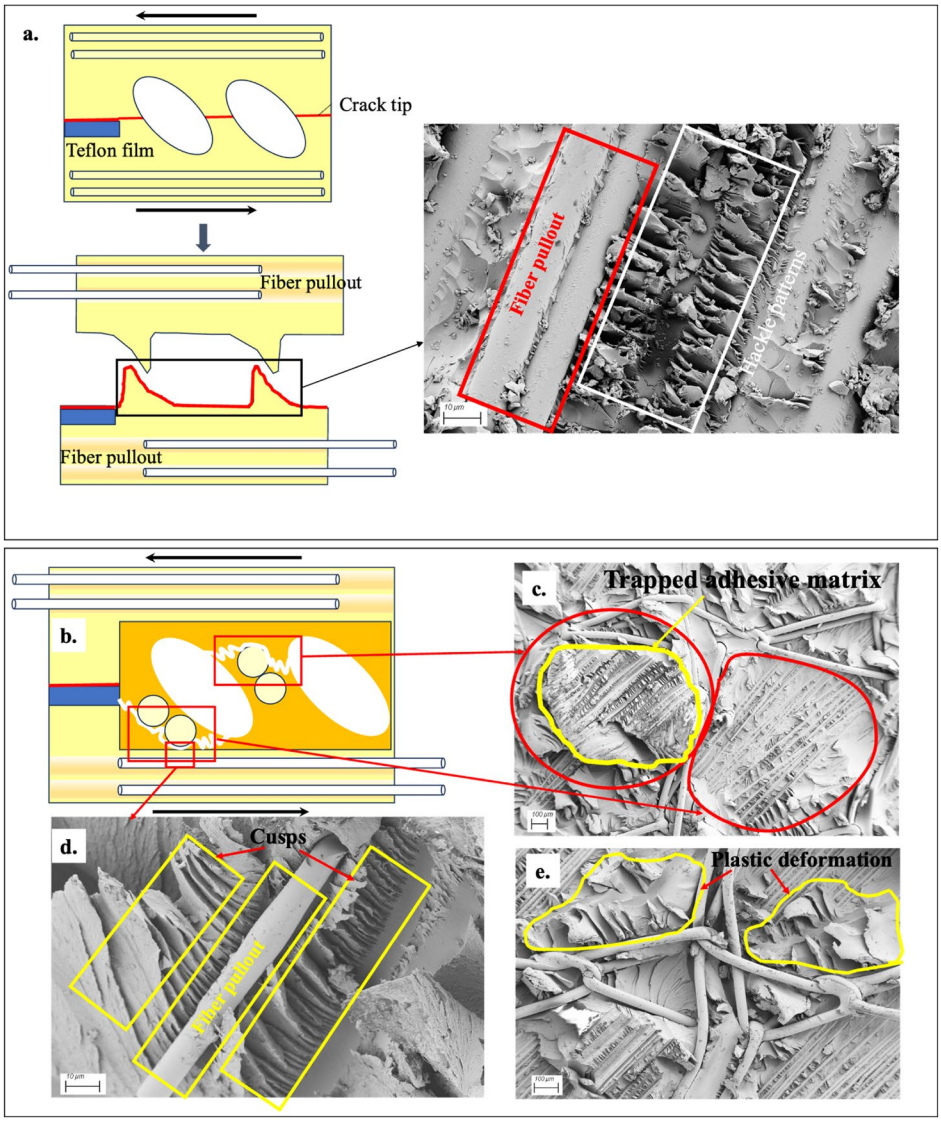

FIGURE 12 | SEM images of fracture surface under mode-II for (a) REF and (b–e) ALE samples, along with schematic representations of fracture mechanisms.

The distribution of carrier fibers—driven by resin flow during the hot press process (Figure S4)—plays a critical role in adhesive thickness variability. Under high pressure and temperature, resin flow redistributes fibers, creating localized clusters or uniform distributions. Clustered fibers enhance toughness by resisting crack advance, while uniform distributions exacerbate interfacial weaknesses, as observed in SEM analysis (Figure 10).

3.4.3 | Mode-II Fractography

Figure 12 schematically illustrates the fracture surface under shear force in Mode-II along with an SEM image for REF and ALE samples. The SEM image in Figure 12a shows hackle patterns aligned with the direction of crack propagation, along with ductile deformation surfaces and fiber pullouts. These features are typical in Mode-II fracture, resulting from the coalescence of sinusoidal-shaped micro-cracks occurring perpendicular to the maximum principal tensile stress in the resin-rich region, as noted in references [31, 42].

In contrast, ALE samples exhibit enhanced fracture behavior: Figure 12b–e illustrate how the adhesive layer creates tortuous crack paths around knit fibers, providing additional resin for plastic deformation and significantly improving G_{IIC} values (Figure 4b). Larger hackles in ALE samples (Figure 12d) indicate stronger interfacial bonding between the main laminate fibers and adhesive matrix, correlating with higher energy absorption during crack growth [5, 60, 78]. Crack propagation in ALE samples occurs through both the adhesive-main matrix interface and the adhesive-adhesive layer interface, evidenced by indentations on fracture surfaces (Figure 12c). The bulk adhesive matrix trapped between knitted fibers in Figure 12c confirms the effectiveness of carrier fibers in restricting of resin flow during hot pressing, thereby preserving the integrity of adhesive film under pressure as depicted schematically in Figure 2. Furthermore, pronounced plastic deformations at knit fiber junctions (Figure 12e) highlight the adhesive layer's role in redistributing shear stresses, enhancing G_{IIC}. These findings again highlight the dual role of knit fibers: inducing crack path tortuosity for energy dissipation and reinforcing interfacial bonding to resist shear-driven failure.

4 | Conclusion

In this study, an adhesive film with knitted fiber carriers is used as an interleave layer for E-glass/epoxy composite components, and DCB and ENF samples are prepared by hot press consolidation and tested under Mode-I and Mode-II fracture tests. Additionally, a transverse tensile test is conducted to investigate the in-plane mechanical properties of the components. The incorporation of the adhesive film led to a substantial enhancement in the fracture toughness of the samples, with improvements of 365.39% and 175.47% observed for initiation and propagation, respectively, in Mode-I, and a 171.5% improvement in Mode-II. However, this improvement came at the expense of a reduction in their in-plane properties.

In Mode-I, the introduction of knit fibers enhances fracture toughness through bridging, enhanced plastic deformation and fiber pullout. However, the presence of knit fibers within the adhesive film imposes constraints on plastic zone diameter at the crack tip, limiting the full utilization of the plastic deformation potential arising from excess resin in the adhesive film. Additionally, varying distribution of knitted fibers within the adhesive matrix, influenced by high compression during manufacturing, resulted in two distinct fracture mechanisms: thin-layer cohesive failure and cohesive failure with two different strain energy release rates in Mode-I fracture (G_{IC}). The interface bonding between knit fibers and the adhesive film epoxy is weaker than the adhesion of composite fibers to the main epoxy. Consequently, when carrier fibers are close enough to each other, crack growth typically occurs at the knit fiber-adhesive film epoxy interface. This leads to random shifts in the fracture mechanism and significant fluctuations in G_{IC} values during crack propagation, thereby limiting the adhesive film's contribution to improving fracture toughness in Mode-I fracture. However, due to the dominant positive effect of the carrier fibers under shear loading, the adhesive film effectively enhances fracture toughness in Mode-II loading.

Author Contributions

Sasan Karimi: conceptualization, methodology, formal analysis, investigation, data curation, visualization, and writing – original draft. **Ali Barzegar:** formal analysis, investigation, data curation, and visualization. **Abdulrahman Al-Nadhari:** formal analysis, investigation, data curation, and visualization. **Andreas Kappel:** conceptualization, methodology, supervision, resources, writing – review and editing. **Christian Mittelstedt:** conceptualization, methodology, resources, writing – review and editing. **Hatice S. Sas:** conceptualization, methodology, supervision, visualization, resources, project administration, writing – review and editing. **Mehmet Yildiz:** conceptualization, methodology, supervision, resources, writing – review and editing.

Acknowledgments

This research did not receive any specific grant from funding agencies in the public, commercial, or nonprofit sectors. The authors appreciate Mr. Hasan Dadaq, Technical Director of the Composite Manufacturing Workshop at the Department of Lightweight Construction and Structural Mechanics, TU Darmstadt, for his support during composite manufacturing.

Conflicts of Interest

The authors declare no conflicts of interest.

Data Availability Statement

The data that support the findings of this study are available from the corresponding author upon reasonable request.

References

1. I. V. Sela and O. Ishai, "Interlaminar Fracture Toughness and Toughening of Laminated Composite Materials: A Review," 20, no. 5 (1989): 423–435.

2. P. K. Mallick, *Fiber-Reinforced Composites Materials, Manufacturing, and Design, Third Edition*, 3rd ed. (CRC Press, 2007), https://doi.org/10.1201/9781420005981.

3. M. H. Nguyen, P. Davidson, and A. M. Waas, "Particle-Toughened Interlayers Enhance Mechanical Response of Composite Laminates," *Composites Science and Technology* 182 (May 2019): 107761, https://doi.org/10.1016/j.compscitech.2019.107761.

4. K. Shivakumar and R. Panduranga, "Interleaved Polymer Matrix Composites—A Review," In *Collection of Technical Papers—AIAA/ASME/ASCE/AHS/ASC Structures, Structural Dynamics and Materials Conference*, 2013:1–13.

5. X. Zhao, W. Chen, X. Han, Y. Zhao, and S. Du, "Enhancement of Interlaminar Fracture Toughness in Textile-Reinforced Epoxy Composites With Polyamide 6/Graphene Oxide Interlaminar Toughening Tackifier," *Composites Science and Technology* 191 (2020): 108094, https://doi.org/10.1016/j.compscitech.2020.108094.%0A.

6. Y. Nakai and C. Hiwa, "Effects of Loading Frequency and Environment on Delamination Fatigue Crack Growth of CFRP," *International Journal of Fatigue* 24, no. 2–4 (2002): 161–170, https://doi.org/10.1016/S0142-1123(01)00069-X.

7. M. Hojo, S. Matsuda, M. Tanaka, S. Ochiai, and A. Murakami, "Mode I Delamination Fatigue Properties of Interlayer-Toughened CF/Epoxy Laminates," *Composites Science and Technology* 66, no. 5 (2006): 665–675, https://doi.org/10.1016/j.compscitech.2005.07.038.

8. S. F. Chen and B. Z. Jang, "Fracture Behaviour of Interleaved Fiber-Resin Composites," *Composites Science and Technology* 41, no. 1 (1991): 77–97, https://doi.org/10.1016/0266-3538(91)90054-S.

9. M. Yasaee, I. P. Bond, R. S. Trask, and E. S. Greenhalgh, "Mode I Interfacial Toughening Through Discontinuous Interleaves for Damage Suppression and Control," *Composites. Part A, Applied Science and Manufacturing* 43, no. 1 (2012): 198–207, https://doi.org/10.1016/j.compositesa.2011.10.009.

10. W. Yan, H. Y. Liu, and Y. W. Mai, "Numerical Study on the Mode I Delamination Toughness of z-Pinned Laminates," *Composites Science and Technology* 63, no. 10 (2003): 1481–1493, https://doi.org/10.1016/S0266-3538(03)00167-2.

11. A. Barzegar, S. Karimi, E. F. Sukur, H. S. Sas, and M. Yildiz, "Effect of Fiber Orientation on Temperature History During Laser-Assisted Thermoplastic Fiber Placement," *Journal of Reinforced Plastics and Composites* 42, no. 17-18 (2022): 953–968, https://doi.org/10.1177/07316844221143448.

12. S. Karimi, P. Y. Louyeh, A. Barzegar, M. Yildiz, and H. S. Sas, "A Study of Post-Processing for AFP-Fabricated Thermoplastic Composites With Void Content and Air Permeability Characterization," *Journal of Reinforced Plastics and Composites* 43, no. 9-10 (2023): 490–503, https://doi.org/10.1177/07316844231166078.

13. A. Barzegar, S. Karimi, H. S. Sas, and M. Yildiz, "Enhancing Interlaminar Bonding Quality Estimation in Laser-Assisted Fiber Placement of CF/PEKK Composites: A Correction Factor Approach for Improved Prediction of Intimate Contact," *Composites Part A-Applied Science and Manufacturing* 181 (2024): 108095, https://doi.org/10.1016/j.compositesa.2024.108095.

14. G. Zhang, J. Ghorbani, X. Zheng, et al., "Anisotropic and Elastoplastic Mode I Fracture Toughnesses of Three Additively Manufactured

Polymers Fabricated via Material Extrusion and Powder Bed Fusion," *Fatigue & Fracture of Engineering Materials & Structures* 46, no. 12 (2023): 4776–4782, https://doi.org/10.1111/ffe.1416.

15. V. Dikshit, S. K. Bhudolia, and S. C. Joshi, "Multiscale Polymer Composites: A Review of the Interlaminar Fracture Toughness Improvement," *Fibers* 5, no. 4 (2017): 38, https://doi.org/10.3390/fib5040038.

16. M. Guo, X. Yi, G. Liu, and L. Liu, "Simultaneously Increasing the Electrical Conductivity and Fracture Toughness of Carbon-Fiber Composites by Using Silver Nanowires-Loaded Interleaves," *Composites Science and Technology* 97 (2014): 27–33, https://doi.org/10.1016/j.compscitech.2014.03.020.

17. R. Palazzetti, A. Zucchelli, C. Gualandi, et al., "Influence of Electrospun Nylon 6,6 Nanofibrous Mats on the Interlaminar Properties of gr-Epoxy Composite Laminates," *Composite Structures* 94, no. 2 (2012): 571–579, https://doi.org/10.1016/j.compstruct.2011.08.019.

18. M. Guo, X. Yi, C. Rudd, and X. Liu, "Preparation of Highly Electrically Conductive Carbon-Fiber Composites With High Interlaminar Fracture Toughness by Using Silver-Plated Interleaves," *Composites Science and Technology* 176 (February 2019): 29–36, https://doi.org/10.1016/j.compscitech.2019.03.014.

19. O. M. Bany Mousa and R. A. Taylor, "A Broad Comparison of Solar Photovoltaic and Thermal Technologies for Industrial Heating Applications," *Journal of Solar Energy Engineering* 141, no. 1 (2018): 011002, https://doi.org/10.1115/1.4040840.

20. D. Quan, R. Alderliesten, C. Dransfeld, N. Murphy, A. Ivanković, and R. Benedictus, "Enhancing the Fracture Toughness of Carbon Fibre/Epoxy Composites by Interleaving Hybrid Meltable/Non-Meltable Thermoplastic Veils," *Composite Structures* 252 (2020): 112699, https://doi.org/10.1016/j.compstruct.2020.112699.

21. H. Caglar, S. Idapalapati, M. Sharma, and K. S. Chian, "Debonding of Carbon Fiber Veil Interleaved Adhesively Bonded GFRP Joints via Joule Heating," *Composites. Part B, Engineering* 230 (2022): 109544, https://doi.org/10.1016/j.compositesb.2021.109544.

22. G. W. Beckermann and K. L. Pickering, "Mode i and Mode II Interlaminar Fracture Toughness of Composite Laminates Interleaved With Electrospun Nanofibre Veils," *Composites. Part A, Applied Science and Manufacturing* 72 (2015): 11–21, https://doi.org/10.1016/j.compositesa.2015.01.028.

23. E. Maccaferri, L. Mazzocchetti, T. Benelli, T. M. Brugo, A. Zucchelli, and L. Giorgini, "Rubbery Nanofibrous Interleaves Enhance Fracture Toughness and Damping of CFRP Laminates," *Materials and Design* 195 (2020): 109049, https://doi.org/10.1016/j.matdes.2020.109049.

24. K. Shivakumar, S. Lingaiah, H. Chen, P. Akangah, G. Swaminathan, and L. Russell, "Polymer Nanofabric Interleaved Composite Laminates," *AIAA Journal* 47, no. 7 (2009): 1723–1729, https://doi.org/10.2514/1.41791.

25. D. Zhang, L. Ye, S. Deng, J. Zhang, Y. Tang, and Y. Chen, "CF/EP Composite Laminates With Carbon Black and Copper Chloride for Improved Electrical Conductivity and Interlaminar Fracture Toughness," *Composites Science and Technology* 72, no. 3 (2012): 412–420, https://doi.org/10.1016/j.compscitech.2011.12.002.

26. W. Zheng, Z. Yao, H. Lin, J. Zhou, H. Cai, and T. Qi, "Improved Fracture Toughness of Carbon Fiber Fabric/Epoxy Composite Laminates Using Polyether Sulfone Fibers," *High Performance Polymers* 31, no. 8 (2019): 996–1005, https://doi.org/10.1177/0954008318812151.

27. J. J. Stahl, A. E. Bogdanovich, and P. D. Bradford, "Carbon Nanotube Shear-Pressed Sheet Interleaves for Mode i Interlaminar Fracture Toughness Enhancement," *Composites. Part A, Applied Science and Manufacturing* 80 (2016): 127–137, https://doi.org/10.1016/j.compositesa.2015.10.014.

28. R. J. Sager, P. J. Klein, D. C. Davis, D. C. Lagoudas, and G. L. Warren, "Interlaminar Fracture Toughness of Woven Fabric Composite Laminates With Carbon Nanotube/Epoxy Interleaf Films," *Journal of Applied Polymer Science* 121, no. 4 (2011): 2394–2405, https://doi.org/10.1002/app.33479.

29. B. AlKhateab, I. E. Tabrizi, J. S. M. Zanjani, et al., "Damage Mechanisms in CFRP/HNT Laminates Under Flexural and In-Plane Shear Loadings Using Experimental and Numerical Methods," *Composites. Part A, Applied Science and Manufacturing* 136, no. May (2020): 105962, https://doi.org/10.1016/j.compositesa.2020.105962.

30. M. K. Singh and R. Kitey, "Enhancing Low Velocity Impact Characteristics of Glass Fiber Laminates by Short Fiber Reinforcement—Failure Evolution and Damage Mechanisms," *Polymer Composites* 43, no. 11 (2022): 8030–8049, https://doi.org/10.1002/pc.26945.

31. M. Ç. Akbolat, K. B. Katnam, C. Soutis, P. Potluri, S. Sprenger, and J. Taylor, "On Mode-I and Mode-II Interlaminar Crack Migration and R-Curves in Carbon/Epoxy Laminates With Hybrid Toughening via Core-Shell Rubber Particles and Thermoplastic Micro-Fibre Veils," *Composites. Part B, Engineering* 238 (2022): 109900, https://doi.org/10.1016/j.compositesb.2022.109900.

32. Y. Huang, Y. Qiu, and Y. Wei, "Composite Interlaminar Fracture Toughness Imparted by Electrospun PPO Veils and Interleaf Particles: A Mechanistical Comparison," *Composite Structures* 312 (2023): 116865, https://doi.org/10.1016/j.compstruct.2023.116865.

33. Q. Chen, F. Wu, Z. Jiang, et al., "Improved Interlaminar Fracture Toughness of Carbon Fiber/Epoxy Composites by a Combination of Extrinsic and Intrinsic Multiscale Toughening Mechanisms," *Composites. Part B, Engineering* 252 (2023): 110503, https://doi.org/10.1016/j.compositesb.2023.110503.

34. N. Zheng, H. Y. Liu, J. Gao, and Y. W. Mai, "Synergetic Improvement of Interlaminar Fracture Energy in Carbon Fiber/Epoxy Composites With Nylon Nanofiber/Polycaprolactone Blend Interleaves," *Composites. Part B, Engineering* 171 (May 2019): 320–328, https://doi.org/10.1016/j.compositesb.2019.05.004.

35. Y. Ou, L. Wu, M. Hefetz, C. González, and V. J. José, "Improving Interlaminar Properties of Woven Carbon Fibre Composite Laminates With Industrial-Scale Carbon Nanotube Fibre Interleaves," *Composites. Part A, Applied Science and Manufacturing* 164 (2023): 107283, https://doi.org/10.1016/j.compositesa.2022.107283.

36. V. S. Uppin, P. S. Shivakumar Gouda, I. Sridhar, M. A. Umarfarooq, and A. Edacherian, "Effects of Carbon/Glass Nonwoven Interleaving Veils and Their Areal Density on Opening and Shearing Mode Interlaminar Fracture Toughness of Glass Epoxy Composites," *Theoretical and Applied Fracture Mechanics* 130 (2024): 104292, https://doi.org/10.1016/j.tafmec.2024.104292.

37. V. S. Uppin, P. S. S. Gouda, I. Sridhar, M. A. Umarfarooq, and A. Edacherian, "Interleaving Carbon-Glass Veils in Glass Epoxy Composite for Enhanced Fracture Toughness and Interlaminar Shear Strength—A Hybrid Approach," *Polymer Composites* 45, no. 12 (2024): 10654–10665, https://doi.org/10.1002/pc.28498.

38. C. Yildirim, H. Ulus, B. Beylergil, A. Al-Nadhari, S. Topal, and M. Yildiz, "Effect of Atmospheric Plasma Treatment on Mode-I and Mode-II Fracture Toughness Properties of Adhesively Bonded Carbon Fiber/PEKK Composite Joints," *Engineering Fracture Mechanics* 289 (2023): 109463, https://doi.org/10.1016/j.engfracmech.2023.109463.

39. X. Qian, O. G. Kravchenko, D. Pedrazzoli, and I. Manas-Zloczower, "Effect of Polycarbonate Film Surface Morphology and Oxygen Plasma Treatment on Mode I and II Fracture Toughness of Interleaved Composite Laminates," *Composites. Part A, Applied Science and Manufacturing* 105 (2018): 138–149, https://doi.org/10.1016/j.compositesa.2017.11.016.

40. L. K. Jain and Y. W. Mai, "Determination of Mode II Delamination Toughness of Stitched Laminated Composites," *Composites Science*

and Technology 55, no. 3 (1995): 241–253, https://doi.org/10.1016/0266-3538(95)00089-5.

41. Y. Tanzawa, N. Watanabe, and T. Ishikawa, "Interlaminar Fracture Toughness of 3-D Orthogonal Interlocked Fabric Composites," *Composites Science and Technology* 59, no. 8 (1999): 1261–1270, https://doi.org/10.1016/S0266-3538(98)00167-5.

42. A. Aksoy and L. A. Carlsson, "Interlaminar Shear Fracture of Interleaved Graphite/Epoxy Composites," *Composites Science and Technology* 43, no. 1 (1992): 55–69, https://doi.org/10.1016/0266-3538(92)90133-N.

43. F. Sacchetti, W. J. B. Grouve, L. L. Warnet, and I. F. Villegas, "Effect of Resin-Rich Bond Line Thickness and Fibre Migration on the Toughness of Unidirectional Carbon/PEEK Joints," *Composites Part A-Applied Science and Manufacturing* 109 (2018): 197–206, https://doi.org/10.1016/j.compositesa.2018.02.035.

44. M. Arai, Y. Noro, K. i. Sugimoto, and M. Endo, "Mode I and Mode II Interlaminar Fracture Toughness of CFRP Laminates Toughened by Carbon Nanofiber Interlayer," *Composites Science and Technology* 68, no. 2 (2008): 516–525, https://doi.org/10.1016/j.compscitech.2007.06.007.

45. N. Sela, O. Ishai, and L. Banks-Sills, "The Effect of Adhesive Thickness on Interlaminar Fracture Toughness of Interleaved Cfrp Specimens," *Composites* 20, no. 3 (1989): 257–264, https://doi.org/10.1016/0010-4361(89)90341-8.

46. S. U. Khan and J. K. Kim, "Improved Interlaminar Shear Properties of Multiscale Carbon Fiber Composites With Bucky Paper Interleaves Made From Carbon Nanofibers," *Carbon* 50, no. 14 (2012): 5265–5277, https://doi.org/10.1016/j.carbon.2012.07.011.

47. M. R. Hosseini, F. Taheri-Behrooz, and M. Salamat-talab, "Mode II Interlaminar Fracture Toughness of Woven E-Glass/Epoxy Composites in the Presence of Mat Interleaves," *International Journal of Adhesion and Adhesives* 98 (2020): 102523, https://doi.org/10.1016/j.ijadhadh.2019.102523.

48. J. Liu, Y. Li, D. Xiang, C. Zhao, B. Wang, and H. Li, "Enhanced Electrical Conductivity and Interlaminar Fracture Toughness of CF/EP Composites via Interleaving Conductive Thermoplastic Films," *Applied Composite Materials* 28, no. 1 (2021): 17–37, https://doi.org/10.1007/s10443-020-09848-w.

49. M. Yasaee, I. P. Bond, R. S. Trask, and E. S. Greenhalgh, "Mode II Interfacial Toughening Through Discontinuous Interleaves for Damage Suppression and Control," *Composites. Part A, Applied Science and Manufacturing* 43, no. 1 (2012): 121–128, https://doi.org/10.1016/j.compositesa.2011.09.026.

50. L. Li, P. Lee-Sullivan, and K. M. Liew, "The Influence of Thermoplastic Film Interleaving on the Interlaminar Shear Strength and Mode i Fracture of Laminated Composites," *Journal of Engineering Materials and Technology* 118, no. 3 (1996): 302–309, https://doi.org/10.1115/1.2806810.

51. F. Narducci, K. Y. Lee, and S. T. Pinho, "Interface Micro-Texturing for Interlaminar Toughness Tailoring: A Film-Casting Technique," *Composites Science and Technology* 156 (2018): 203–214, https://doi.org/10.1016/j.compscitech.2017.10.016.

52. M. Hojo, "Thickness Effect of Double Cantilever Beam Specimen on Interlaminar Fracture Toughness of AS4/PEEK and T800/Epoxy Laminates," 1993, https://doi.org/10.1520/STP24736S.

53. M. Hojo, S. Ochiai, C.-G. Gustafson, and K. Tanaka, "Effect of Matrix Resin on Delamination Fatigue Crack Growth in CFRP Laminates," *Engineering Fracture Mechanics* 49 (1994): 35–47.

54. K. Friedrich, *Application of Fracture Mechanics to Composite Materials*, 1st ed., ed. K. Friedrich (Elsevier Science, 1989).

55. N. Odagiri, H. Kishi, and M. Yamashita, "Development of TORAYCA Prepreg P2302 Carbon Fiber Reinforced Plastic for Aircraft Primary Structural Materials," *Advanced Composite Materials* 5 (1996): 249–252, https://doi.org/10.1163/156855196X00301.

56. S. Matsuda, M. Hojo, S. Ochiai, A. Murakami, H. Akimoto, and M. Ando, "Effect of Ionomer Thickness on Mode I Interlaminar Fracture Toughness for Ionomer Toughened CFRP," *Composites. Part A, Applied Science and Manufacturing* 30, no. 11 (1999): 1311–1319, https://doi.org/10.1016/S1359-835X(99)00023-8.

57. X. Xu, Z. Zhou, Y. Hei, B. Zhang, J. Bao, and X. Chen, "Improving Compression-After-Impact Performance of Carbon-Fiber Composites by CNTs/Thermoplastic Hybrid Film Interlayer," *Composites Science and Technology* 95 (2014): 75–81, https://doi.org/10.1016/j.compscitech.2014.01.023.

58. L. Daelemans, S. van der Heijden, I. De Baere, H. Rahier, W. Van Paepegem, and K. De Clerck, "Improved Fatigue Delamination Behaviour of Composite Laminates With Electrospun Thermoplastic Nanofibrous Interleaves Using the Central Cut-Ply Method," *Composites. Part A, Applied Science and Manufacturing* 94 (2017): 10–20, https://doi.org/10.1016/j.compositesa.2016.12.004.

59. S. Singh and I. K. Partridge, "Mixed-Mode Fracture in an Interleaved Carbon-Fibre/Epoxy Composite," *Composites Science and Technology* 55, no. 4 (1995): 319–327, https://doi.org/10.1016/0266-3538(95)00062-3.

60. M. Idrees, G. R. Palmese, and N. J. Alvarez, "Maximizing the Interlaminar Fracture Toughness of Thermoset Interleaved Woven Glass Fiber Laminates," *Composites Part A-Applied Science and Manufacturing* 172 (2023): 107616, https://doi.org/10.1016/j.compositesa.2023.107616.

61. J. E. Masters, "Improved Impact and Delamination Resistance Through Interleafing," *Key Engineering Materials* 37 (1989): 317–347, https://doi.org/10.4028/www.scientific.net/kem.37.317.

62. M. Idrees, A. M. H. Ibrahim, E. Tekerek, A. Kontsos, G. R. Palmese, and N. J. Alvarez, "The Effect of Resin-Rich Layers on Mechanical Properties of 3D Printed Woven Fiber-Reinforced Composites," *Composites Part A-Applied Science and Manufacturing* 144 (2021): 106339, https://doi.org/10.1016/j.compositesa.2021.106339.

63. M. Hojo, S. Matsuda, S. Ochiai, A. Murakami, and H. Akimoto, "The Role of Interleaf/Base Lamina Interphase in Toughening Mechanism of Interleaf-Toughened Cfrp," ICCM-12 Conf., 1999.

64. Y. A. Resis and D. H. Reneker, "Delamination Composites Prepared by Small Diamerter Fiber Reinforcement at Ply Interface," 2001, 1 (12), http://www.google.com/patents/US6265333.

65. ASTM D5528-01, "Standard Test Method for Mode I Interlaminar Fracture Toughness of Unidirectional Fiber-Reinforced Polymer Matrix Composites," ASTM, 2014: 1–12.

66. ASTM D7905, "Standard Test Method for Determination of the Mode II Interlaminar Fracture Toughness of Unidirectional Fiber-Reinforced Polymer Matrix Composites," ASTM, 2014: 1–18.

67. ASTM D3039, "Standard Test Method for Tensile Properties of Polymer Matrix Composite Materials," *ASTM* 15 (2014): 1–13.

68. M. Seyyednourani, S. Akgun, H. Ulus, M. Yildiz, and H. S. Sas, "Experimental Investigation on Compression-After-Impact (CAI) Response of Aerospace Grade Thermoset Composites Under Low-Temperature Conditions Assisted With Acoustic Emission Monitoring," *Composite Structures* 321, no. May (2023): 117260, https://doi.org/10.1016/j.compstruct.2023.117260.

69. A. Yudhanto, M. Alfano, and G. Lubineau, "Surface Preparation Strategies in Secondary Bonded Thermoset-Based Composite Materials: A Review," *Composites Part A-Applied Science and Manufacturing* 147 (2021): 106443, https://doi.org/10.1016/j.compositesa.2021.106443.

70. F. Ozdil and L. A. Carlsson, "Plastic Zone Estimates in Mode I Interlaminar Fracture of Interleaved Composites," *Engineering Fracture Mechanics* 41, no. 5 (1992): 645–658, https://doi.org/10.1016/0013-7944(92)90151-4.

71. "3M. Structural Adhesive Film," 2007, 1–15.

72. O. Rodera, J. Jokinen, O. Orell, L. George, N. Pournoori, and M. Kanerva, "Multi-Layer Continuum Model for Adhesive Films With Knitted Carrier," *Composites Science and Technology* 236 (2023): 109981, https://doi.org/10.1016/j.compscitech.2023.109981.

73. M. Naderi, N. Apetre, and N. Iyyer, "Effect of Interface Properties on Transverse Tensile Response of Fiber-Reinforced Composites: Three-Dimensional Micromechanical Modeling," *Journal of Composite Materials* 51, no. 21 (2017): 2963–2977, https://doi.org/10.1177/0021998316681189.

74. F. Ozdil and L. A. Carlsson, "Mode I Interlaminar Fracture of Interleaved Graphite/Epoxy," *Journal of Composite Materials* 26, no. 3 (1992): 432–459, https://doi.org/10.1177/002199839202600306.

75. E. J. Pappa, J. A. Quinn, J. J. Murray, and J. R. Davidson, "Experimental Study on the Interlaminar Fracture Properties of Carbon Fibre Reinforced Polymer Composites With a Single Embedded Toughened Film," *Polymers (Basel)* 13, no. 23 (2021): 4103, https://doi.org/10.3390/polym13234103.

76. C. Cheng, C. Zhang, J. Zhou, et al., "Improving the Interlaminar Toughness of the Carbon Fiber/Epoxy Composites via Interleaved With Polyethersulfone Porous Films," *Composites Science and Technology* 183 (2019): 107827, https://doi.org/10.1016/j.compscitech.2019.107827.

77. N. H. Nash, T. M. Young, and W. F. Stanley, "The Reversibility of Mode-I and -II Interlaminar Fracture Toughness After Hydrothermal Aging of Carbon/Benzoxazine Composites With a Thermoplastic Toughening Interlayer," *Composite Structures* 152 (2016): 558–567, https://doi.org/10.1016/j.compstruct.2016.05.086.

78. B. Jony, S. B. Mulani, and S. Roy, "Interlaminar Shear Fracture Healing of Thermoset CFRP Composite Using Multiphase Thermoplastic Healing Agents," *Composite Structures* 279, no. August 2021 (2022): 114807, https://doi.org/10.1016/j.compstruct.2021.114807.

Supporting Information

Additional supporting information can be found online in the Supporting Information section.